Experimental and Numerical Investigation of a Multi-Jet Impingement Cooling Configuration

M. Schroll[1,*], J. Klinner[1], M. Müller[1], M. Matha[2], M. Hilfer[3], S. Tabassum[4], C. Morsbach[2], R. Brakmann[4], C. Willert[1,*]

1: Institute of Propulsion Technology (Measurement Techniques), German Aerospace Center (DLR), Köln, Germany
2: Institute of Propulsion Technology (Numerical Methods), German Aerospace Center (DLR), Köln, Germany
3: Institute of Aerodynamics and Flow Technology (Experimental Methods), German Aerospace Center (DLR), Göttingen, Germany
4: Institute of Propulsion Technology (Turbine), German Aerospace Center (DLR), Göttingen, Germany
*Corresponding author: michael.schroll@dlr.de

Keywords: turbine blade cooling, jet impingement, flow (dynamics), heat transfer, jets, cross-flow, temperature, turbulence, computational fluid dynamics, RANS, large eddy simulation, LES, Reynolds-averaged Navier-Stokes equations, high-speed PIV, time-resolved PIV, unsteady temperature sensitive paint, iTSP

ABSTRACT

In order to protect turbine blades from thermal damage or thermally induced aging, internal impingement cooling has found common use throughout engine design, both in stationary gas turbines as well as aircraft engines, but also finds applications in other areas requiring cooling. The present investigation is focused on a generic impingement cooling configuration that can be easily modelled with computational fluid dynamics (CFD) and at the same time can be studied in detail experimentally. The acquired experimental data can be directly used for the validation of the CFD simulations, ultimately allowing their application in more complex, realistic configurations where experimental investigations become prohibitively expensive or otherwise impossible. The investigated configuration consists of 9 evenly spaced jets of Reynolds number $\mathrm{Re}_D = 10\,000$ issuing into a square channel that is sealed at one end. The jets directly impinge on a uniformly heated target plate. With previous work on similar configurations well described in literature, the focus of the present contribution is to further exploit the potentials offered by snap-shot based and time-resolved measurements. The flow field within the channel is characterized with both conventional, snap-shot particle image velocimetry (PIV) as well as with high-speed, time-resolved PIV (TR-PIV) to, respectively, capture overview data as well as detailed information on temporally evolving flow structures. In addition, measurements of the unsteady surface temperature distribution on the heated channel wall are performed by means of a newly developed unsteady temperature sensitive paint (iTSP) measurement technique. The interaction of the turbulent jets with the wall and with its neighbors is studied in detail using correlation and spectral analysis as well as modal decomposition. Where possible, this is supplemented with corresponding data obtained from numerical modelling. None of the applied post-processing methods reveal a significant interaction between jets suggesting that the jet-driven dynamics of heat transfer at the wall are restricted to their immediate vicinity which may simplify the requirements on numerical models of similar cooling configurations.

1. Introduction

In order to protect turbine blades from thermal damage or thermally induced aging, internal impingement cooling has found common use throughout engine design, both in stationary gas turbines as well as aircraft engines, but also finds applications in other areas requiring cooling. This form of active cooling relies on diverting compressed air from the engine (or some other source) which lowers its overall efficiency. The aim of increased efficiency implies reductions of cooling air use that can only be achieved through improvements of the cooling efficiency. This aim is further compounded by increased combustion chamber exit temperatures as a consequence of increased cycle temperatures. Within this context, impingement cooling is a very common configuration in which small jets of cooler air impinge on the inner surface of the turbine blade resulting in convective (forced) cooling of the inner surface and adjoining material. Spent cooling air is typically released through small holes of the surface of the blade creating an additional thermal protection (effusive cooling) or through holes from the blade's trailing edge.

The present investigation is focused on a generic impingement cooling configuration that can be easily modelled with computational fluid dynamics (CFD) and at the same time can be studied in detail experimentally. The acquired experimental data can be directly used for the validation of the CFD simulations, ultimately allowing their application in more complex, realistic configurations where experimental investigations become prohibitively expensive or otherwise impossible.

The presently investigated configuration consists of 9 evenly spaced jets of Reynolds number $\mathrm{Re}_D = 10\,000$ issuing into a square channel that is sealed at one end. The jets directly impinge on a heated side wall of the channel. Previous work on similar configurations are described in Brakmann et al. (2016); Gaffuri et al. (2019); Hossain et al. (2018); Y. Rao et al. (2016); Terzis (2016). The purpose of the present contribution is to further exploit the potentials offered by snap-shot based and time-resolved measurements. In particular, the flow field within the channel is characterized with both conventional, snap-shot particle image velocimetry (PIV) as well as with high-speed, time-resolved PIV (TR-PIV), to respectively capture overview data as well as detailed information on temporally evolving flow structures. Measurements of the unsteady surface temperature distribution on the heated channel by means of the unsteady temperature sensitive paint (iTSP) technique aim at uncovering the temperature dynamics on the wall.

The experiments described herein are accompanied with CFD based on Reynolds-averaged Navier-Stokes simulation (RANS) and large-eddy simulation (LES). While briefly described herein, more details on the CFD modelling of the present configuration along with results can be found in Tabassum et al. (2022).

The paper is structured as follows: The next sections provide an overview of the problem statement along with a literature review. Section 2 describes the experimental configuration chosen for the study along with the various measurement techniques employed to assemble an extensive experimental data base. Section 3 provides information on the corresponding CFD modelling of the configuration. The results Sect. 4 discusses various approaches of the extracting information

from the time-resolved measurement data beyond the classical statistics and, where possible, is compared to the RANS and LES data base.

1.1. The impingement jet problem

An impinging jet on a flat plate has many complex flow effects (free jet - , stagnation - and wall jet region) within a relatively simple geometry, hence the impingement jet problem is excellently suited for test, validation and development of numerical and experimental methods. The flow configuration is outlined in Fig. 1. In the free jet region, the air moves away from the nozzle exit with shear layers forming between the jet and the ambient surrounding fluid. Vortices are shed from the shear layer having entrained large amounts of ambient fluid and reducing the jet's axial velocity. The central part of the jet (where the original velocity is maintained) is called potential core. Depending on the Reynolds number and a variety of other factors the potential core typically extends up to $4-5\,D$. As the jet begins to "feel" the target plate, it enters a stagnation region where the axial velocity component decreases until reaching zero and is then deflected in radial direction parallel to the wall. The boundary layer in this region is very thin with a typical thickness of $\delta \leq 0.01\,D$. This region is characterized by an adverse pressure gradient, high streamline curvature, as well as high normal and shear stresses. These complexities make it very difficult to numerically predict the stagnation region with a (simple) turbulence model. The wall jet is surrounded by a boundary layer at the target plate and a shear layer to the surrounding the fluid. The wall jet velocity typically achieves a maximum at $1\,D$ from the stagnation zone. The wall jet eventually passes from laminar to turbulent. At a distance of $2.5\,D$ from the impinging point the velocity is considered as self-similar, similarity for the turbulent quantities is reached at $4.5\,D$. In contrast to a wall parallel flow the wall jet has two shear layers (one at the plate and one with the ambient fluid) which lead to much higher turbulence levels. A jet in cross flow or multi jet configuration, such as investigated herein, adds more complexity to the problem. There is an interaction of jets before and after impingement and a collision of wall jets, leading to an upwash area or fountain flow. The spent air from upstream jets leads to cross flow which is increases toward the channel exit for each additional jet.

1.2. Literature review

Various well-written reviews about impingement jet cooling on smooth and flat target surfaces exist. Experimental results for heat and mass transfer of single and multiple-jet impingement configurations are summarized by Martin (1977). Jambunathan et al. (1992) provide a description on the effects of a wide range of parameters on heat transfer in single-jet impingement. The heat transfer characteristics of single and multiple isothermal turbulent air and flame jet impingement with an emphasis on physical phenomena can be found in Viskanta (1993). Zuckerman & Lior (2006) and Dewan et al. (2012) concentrated on the physics, correlations and the strengths and drawbacks of RANS-based turbulence models and LES, respectively. Heat transfer characteristics of systems of

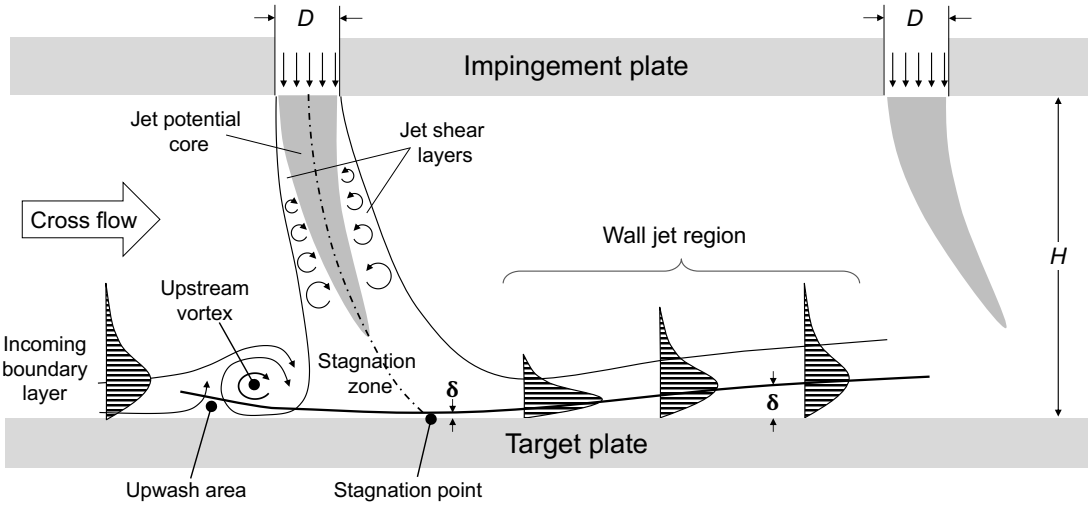

Figure 1. Schematic of the studied jet impingement flow (not to scale).

multiple impinging jets as well as recent developments of suited measurement techniques and numerical accuracy are summarized by Weigand & Spring (2011). Amano & Sundén (2014) reviews state-of-the-art and advanced impingement cooling technologies for gas turbine applications.

The spatio-temporal fluctuation of the impingement jet has not received much attention in literature, even less so for multi jet arrangements and possible interactions between the jets. Hall & Ewing (2004) identified large scale periodic structures on a single impingement jet in the wall jet region ($r/D > 1$) using two-point and two-time correlation measurements of surface pressure fluctuation. These unsteady vortex structures were not necessarily axisymmetric ring structures. The measurements indicated that large scale structures became more periodic and prominent with higher jet Reynolds number. Hadziabdic & Hanjalic (2008) performed an LES study on a single jet ($z/D = 2$ and $\mathrm{Re}_D = 20\,000$) to gain insight into the flow, the coherent and turbulent structures as well as their effect on the heat transfer. They found a tilting and breaking vortex ring around the jet as well as a flapping jet. They also observed a splitting and pairing of the stagnation point - occasionally two stagnation points or a separation line appeared. They describe a locally unsteady flow, including flow reversals and the pairing and branching of streaks in the wall jet region. The shapes of the near wall flow structures suggest that they originate from the large-scale structures caused by the free jet shear layer which are distorted from the impingement onto the target plate. Near wall eddies appear as re-circulation bubbles and are further stretched and eventually entrained into the wall jet. Their presence increases the turbulence above the level that would be expected for a wall parallel flow. Kataoka et al. (1987) reports a surface renewal effect in the stagnation zone driven by turbulence. Dairay et al. (2015) performed a detailed direct numerical simulation (DNS) of a single jet with a wall separation distance of $z/D = 2$ and $\mathrm{Re}_D = 10\,000$. The ring vortices are subjected to distortions while approaching the target plate and produce radially elongated structures at a smaller scale. These small structures are responsible for very high local heat transfer spots on the target plate. The authors linked the flow reversal to high Nusselt number areas and observed propagating cold and hot fronts due to these ring vortices. An LES of a single jet ($z/D = 2$

and $\mathrm{Re}_D = 23\,000$) by Uddin et al. (2013) revealed anisotropic flow in the jet. The nature of the turbulence in the near wall region changes from an axisymmetric contraction state in the stagnation zone to a two-component state in the wall jet region. The ring vortices strike the target plate with a low pressure zone and force the flow into an alternating acceleration and deceleration. In a range around the stagnation point of $1.4 < r/D < 2.8$, the elongated coherent structures cause an upwash at some locations. The developing turbulent thermal boundary layer is characterized by alternating hot and cold spots. Near wall measurements at $z/D = 0.001$ ($D = 37$ mm) by Tummers et al. (2011) indicate that instantaneous flow reversals occur for $r/D > 1.3$ in an approximately $0.005\,D$ thick layer above the impingement plate. They could show that these flow reversals are related to the formation of small secondary vortices. The location of the maximum flow reversal and the minimum Nusselt number are identical, suggesting that the flow reversal is connected to a reduction in heat transfer.

One of the first studies on multi jet impingement (two jets) with LES was conducted by Rizk & Menon (1988). They identified large axisymmetric vortex rings which impinge and propagate above the target. During that propagation a region of secondary vorticity appears upstream of the primary vortex core. When two vortex rings of adjacent jets collide, they are lifted by the resulting fountain flow and are eventually re-entrained into the jet. This also affects the jet spreading. Penumadu & Rao (2017) investigated a basic generic configuration (similar to ours) with LES and validated the simulation with an experiment from G. A. Rao et al. (2009). They observed fluctuating jets due to a high cross flow velocity. An enhancement of local heat transfer at x/D = -1 from the stagnation point due to surface renewal effect caused by the wall jet collision was observed. The correspondence between flow structures and convective heat transfer augmentation was experimentally investigated by Terzis (2016) for a narrow impingement channel at low separation distances ($z/D = 2-3$), using high-resolution PIV measurements and surface heat transfer experiments (Transient Liquid Crystal - TLC). At moderate cross flow they observe that an upstream vortex locally enhances the convection coefficients as it wraps around the jet similar to a horseshoe vortex. Heat transfer coefficients have a local maximum in the vortex downwash and not directly beneath the vortex core (location with maximum shear stress). Some flow features could be identified with the help of a visualization method described by Terzis et al. (2015), which evaluates the distributions of the exponent m in the equation $\mathrm{Nu} \propto \mathrm{Re}^m$. This method revealed the centre of the upstream vortex which shows a local maximum of the exponent m and the actual impingement jet area where m experiences laminar values in the vicinity of the potential core.

The configuration chosen for the present investigation intends to match previous studies in which flow and heat transfer effects have been investigated. Due to previous limitations in computational time and available measuring techniques a full picture of the (fluctuating) impingement jet problem in narrow channels has not been accessible. The presented results help to improve the understanding and prediction of the physics of impingement jets in narrow channels. The unsteady motion of the jet enhances local velocity fluctuation and shear stress; hence this is one more mechanism which leads to increased heat transfer in the stagnation zone of the impingement jet. However, this phenomenon was not often discussed in literature. The present study helps to com-

plete the picture of the impingement jet problem and therefore uses a geometry often studied in literature.

Furthermore, this will help cooling designers in applying innovative cooling methods by exploiting the arbitrary or preferential movement of the jets, e.g. by using fluidic devices in the impingement configurations as suggested by Dutta & Singh (2021). An intensified jet movement might widen the stagnation zone, which leads to a less pronounced hot spot effect and more uniform heat transfer distribution.

2. Experimental Setup and Methods

A schematic of the experimental implementation of the jet impingement cooling configuration is given in Fig. 2. A single row of 9 jets of diameter $D = 15.2\,\text{mm}$ issue into a square channel of side length $H = 76.0\,\text{mm} = 5\,D$. The length to diameter ratio of the jet tubes of $l_{\text{nozzle}}/D = 3$ with both entry and exit of the tubes sharp-edged. The jets are positioned on the channel centerline and are uniformly spaced with a pitch of $p = 5\,D$. The square channel has a length of $L = 900\,\text{mm} \approx 60\,D$ and is attached to a suction system via 4 orthogonal exit tubes at the downstream end. The upstream end of the channel is sealed. The wall opposite to the jets, the *target plate*, consists of a solid aluminum block that is removable and can be electrically heated using a heating foil.

The origin of the Cartesian coordinate system is located on the target plate centered with the axis of jet No. 7. Here the x-axis is aligned with the extent of channel pointing toward its exit. The y-axis aligns with the spanwise direction of the target plate, while the z-axis is normal to the plate. In this configuration the jets issuing into the channel will have a negative mean velocity W while the mean bulk flow moves along the x-axis with velocity component U. Correspondingly, the spanwise velocity component is denoted with V.

Measurement data and CFD results are normalized by the jet diameter D as a characteristic length and the centerline velocity of jet No. 1, U_{jet}, as a characteristic velocity. A reference time is given by the ratio $T_{\text{ref}} = D/U_{\text{jet}}$. The temperature is referenced against the temperature in the plenum supplying the jets.

Photographs of the realized jet impingement cooling configuration are presented in Figure 3. The channel has large optical grade windows with access from all sides, including the upstream and downstream ends, thereby allowing measurements in direct proximity of the walls. The removable target plate can be fitted with either a heating block or a large glass window. The latter is used only for flow field measurements (PIV) of the xy-planes. The orifice plate also contains a miniaturized IR-camera (FLIR Lepton 3.0, LWIR, 160×120 pixels) between jet No. 7 and jet No. 8 that observes the target plate area between the two jets. The 9 jets issuing into the channel are supplied with air from a large plenum that contains flow conditioning based on flow straightening tubes and screens which are mounted upstream of the plenum's convergent section. Static pressure and temperature sensors throughout the rig along with a mass flow meter (orifice plate) allow accurate monitoring

of the flow conditions. The entire setup including the attached large plenum is mounted on a motorized 2-axis translation stage that permits straightforward sectioning of the flow field once optical instrumentation such as camera and laser light sheet have been aligned.

a)

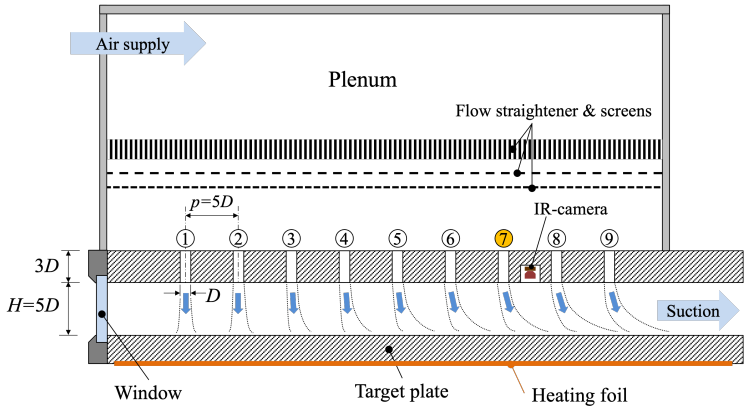

b)

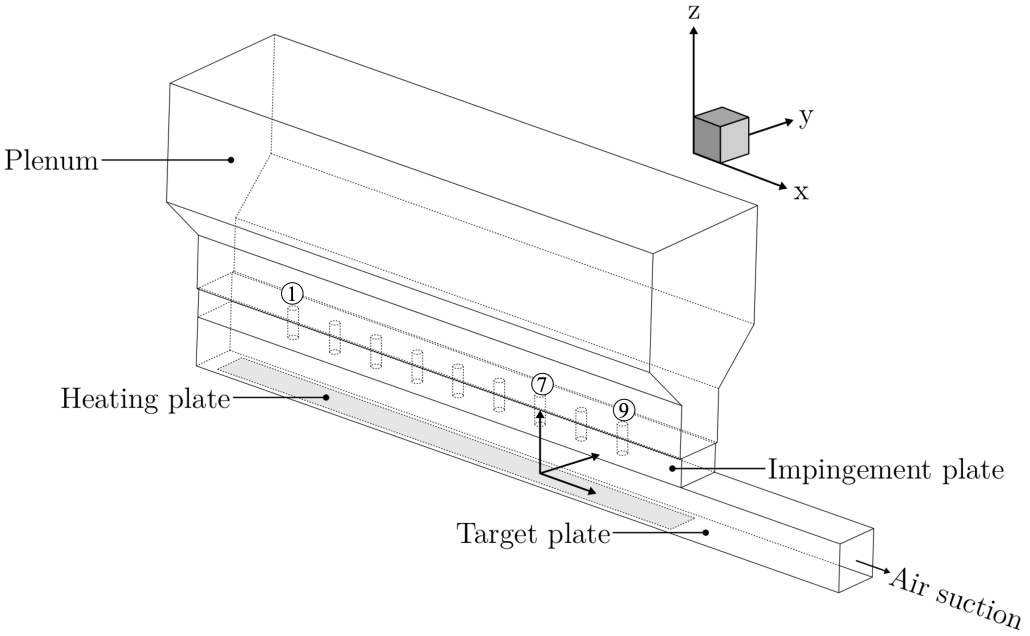

Figure 2. **a** longitudinal section of the multi-impingement jet configuration, **b** schematic of the setup including coordinate system.

2.1. PIV Instrumentation

Detailed data of the flow field is acquired using two-dimensional (planar), two component particle image velocimetry (2D-2C-PIV) using both conventional (snap-shot) PIV as well as TR-PIV. Paraffin droplet-based seeding of $\approx 1\,\mu m$ diameter from an atomizer is added to the flow upstream of the plenum allowing it to be homogeneously distributed once it reaches the jet nozzles. Based on the expected flow conditions of $W_{jet} \approx 10\,m/s$, the Stokes number is estimated to be of order (0.01) indicating that the $\approx 1\,\mu m$ droplets faithfully follow the flow.

The snapshot PIV system comprises a conventional, dual-oscillator, frequency doubled, pulsed Nd:YAG laser (Quantel Evergreen) with a pulse energy of 2×100 mJ and double pulse repetition rate of 25 Hz. The light scattered by the seed droplets is imaged by a sCMOS camera (ILA_5150 GmbH, 2560×2048 pixel, 6.5 µm pitch) using image magnifications between 0.083 and 0.164.

For TR-PIV an industrial grade diode-pumped laser (Innolas Photonics, Nanio-Air 532-10-V-SP) with an integral power of 10 W illuminates the seeding droplets at pulse repetition rates of 20 kHz to 40 kHz. Multiple records of 10 000−60 000 images are acquired with a high-speed CMOS camera (Vision Research V1840, 2048×1952 pixel, 13.5 µm pitch) using magnifications between 0.5 and 0.95. The field of view or region of interest (ROI) is restricted to $3.70\,x/D \times 0.39\,z/D$ and reduces to $1.85\,x/D \times 0.17\,z/D$ when imaging with near unity magnification. The TR-PIV recordings are processed using an in-house, multiple-frame cross-correlation algorithm that utilizes up to 5 recordings per time-step on a coarse-to-fine resolution pyramid (Lynch & Scarano, 2013; Raffel et al., 2018). Data validation is based on the normalized median filter (Westerweel & Scarano, 2005) with a threshold of 2.5−3.0. For the analysis of the near-wall flow the PIV interrogation window (IW) was reduced to 32×8 pixel (0.45×0.08 mm^2).

Table 1. Summary of acquired PIV data.

	Overview	TR-PIV		
Light sheet orientation	xz	xz	xz	xy
Sampling rate [Hz]	25	32 000	20 000	20 000
Sample size N	3000	37 390	58 819	58 819
Record length [s]	120	1.17	2.94	2.94
Number of records	1	3	5	3
Number of ROIs	5	4	1	2
Magnification m	0.082	0.985	0.222	0.208
ROI [pixel]	2560×1152	2048×216	2048×416	2048×416
ROI [mm^2]	202×91	55.3×5.9	124×25.2	133×27.0
ROI [D^2]	13.3×6.0	3.6×0.39	8.2×1.6	8.7×1.8
IW-area [pixel]	24×24	16×16	24×16	24×24
IW-area [mm^2]	1.89×1.89	0.22×0.22	1.46×0.97	1.56×1.56
Grid spacing [mm^2]	0.95×0.95	0.082×0.082	0.73×0.49	0.78×0.78

2.2. iTSP / iPSP Instrumentation

While steady-state implementations of the pressure sensitive paint (PSP) and temperature sensitive paint (TSP) techniques are well established (T. Liu et al., 2021), their extension to provide unsteady measurement data up into the kHz regime is a very recent development (Behn et al., 2021; Gößling et al., 2020; Schramm & Hilfer, 2020). The present application is particular challenging due to the expected small pressure fluctuations of O (1−20 Pa) and small temperature variations of O (0.1−5 K). Whereas unsteady pressure sensitive paint (iPSP) was recently demonstrated for an acoustic sound field (Gößling et al., 2020) and for a jet impinging on an inclined plate (X. Liu et al., 2022), the dynamic pressures for these applications were in the 10−1 000 Pa range which is consid-

erably higher than in the present configuration. Therefore, the possible use of iPSP was ruled out in favor of optimizing the iTSP technique for the current configuration.

For the experiments presented in this paper, an iTSP with high sensitivity, high emission intensity and small coating thickness had to be applied in order to resolve the low-temperature fluctuations. Schramm & Hilfer (2020) reported on the experimental investigation of response time of Ru(phen) and polyamide-based type iTSP with temperature sensitivities above 5%/K and overall TSP-layer response time τ around 3 µs. A similar formulation of the paint is used in experiments presented in this paper. The paint is based on Ru(phen), Dichlorotris (1,10-phenanthroline) Ruthenium(II) hydrate 98%, with a lifetime of 1 µs fixed in a matrix consisting of oxygen-non-permeable polymer, a modified Nylon. This type of Nylon is modified by the manufacturer to be soluble in alcohol. The Ru(phen) based paint can be excited over a range of wavelengths with a maximum around 450−460 nm. Emission maximum of Ru(phen) is found around 600 nm. The active layer of the iTSP is excited using an array of high-power LEDs (Osram Ostar LE-B-P3MQ, $\lambda = 460$ nm) operated in cw mode. The custom made LEDs are equipped with a band-pass filter around the center wave length to separate the excitation and emission light (450 nm $\pm$20 nm). The fluorescence from the paint is imaged with a high-speed CMOS camera (Vision Research V1840, 2048$\times$1952 pixel, 13.5 µm pitch) at either 2 kHz or 4 kHz. To improve SNR, 2$\times$2 pixel binning is partially used. A bandpass filter on the camera lens reduces interference with the excitation light source (630 nm $\pm$38 nm). A photograph of the iTSP imaging setup is provided in Fig. 5 with camera obliquely viewing the TSP surface. The Scheimpflug imaging configuration is applied to ensure focus throughout the field of view in combination with a 50 mm lens (Nikon Nikkor Z 50 mm 1:1.2). An array of 8 LEDs illuminate the surface from the other side of the channel.

The fluctuations of the natural wall temperature between the different flow regimes in our experiment is on the order of 0.1 K. In order to evaluate the temperature fluctuations imposed by the impinging jet on the wall, a heating or cooling of the model or the medium is required. In this work, a heating of the model surface is accomplished using sprayable carbon nanotubes (CNT) heating layer as developed by Klein et al. (2017). This sprayable heating layer allows for highly homogeneous heating delivered immediately at the surface of the model with heating powers of up to $\dot{q} = 5\,\mathrm{kW/m^2}$. The thickness of the CNT layer was adjusted according to a desired electric resistance to $\approx$40 µm. Voltage of up to 120 Volt are typically required to heat up the surface. The layered composition of such TSP-configuration is schematically outlined in Fig. 4.

Several steps are necessary to extract the temperature data from the acquired high-speed image data. A significant fixed frequency signal introduced by the camera is present at 80 Hz and is removed using a notch filter. Robust principal component analysis (RPCA) (Candès et al., 2011) is then used to separate the weak temperature signal from broadband noise, which is mainly introduced by the sensor itself. Image back-projection is applied to map the oblique camera view back to a rectilinear geometry of the target plate. Using a calibration coefficient determined through "flow-off" measurements, the conditioned intensity signal is converted to temperature.

Fig. 6 shows the temperature fluctuations on the target plate and is compiled from 5 different iTSP

measurements. A corresponding profile extracted along the centerline ($y = 0$) gives an indication of the repeatability of the measurements: in the overlapping areas the deviation of the RMS-values is on the order of 0.01 K. Given a change of luminosity of 2.85%/K the measured temperature fluctuation is on the order of 1 count on the 12 bit range (4096 counts) of the high-speed camera.

3. Numerical Setup

Both RANS and LES have been employed to investigate the flow field numerically using TRACE (Geiser et al., 2019), DLR's flow solver for turbomachinery applications. Tabassum et al. (2022) presented the numerical setup and provide at detailed discussion on the ability of RANS and LES to predict the steady state flow field. Since the current contribution focuses on the analysis of the unsteady flow field, only a brief summary of the setup for RANS and LES is given herein.

3.1. Steady-RANS Simulations

The computational domain replicates the experimental setup, with an extended outlet to avoid the reflection of boundary conditions on the jets. The working fluid is an ideal gas (R = 287 J/kgK and γ = 1.4). The viscosity of the fluid is modeled with Sutherlands law of viscosity and the Prandtl number equals 0.71. All walls are treated as adiabatic, while the heated target plate is modelled with a constant heat flux boundary condition, introducing $\dot{q} = 5\,000\,\mathrm{W/m^2}$ into the domain. An inlet boundary condition is assigned at the plenum with a total temperature and a total pressure of 298.2 K and 102 099 Pa respectively. The inlet conditions are persistent throughout the simulations with a turbulence intensity of 1% and the turbulent length scale of 0.003 m. The mass flow rate at the outlet is set for an average jet Reynolds number of 10 000. The k-ω SST turbulence model (Menter et al., 2003) with the inclusion of a transition model from Langtry & Menter (2009) and turbulence energy production limiter by Kato & Launder (1993) is used. The turbulent scalar flux modeling is performed based on Reynolds analogy, for a constant turbulent Prandtl number of 0.9.

Convergence and Grid Quality

The unstructured grid with tetrahedral elements is generated using the software CENTAUR. The mesh for the RANS simulation contains $19.6 \cdot 10^6$ grid cells. The grid convergence index (GCI) based on Richardsons extrapolation (Roache, 1994) is used to address the errors arising purely from the computational mesh sizes. The Nusselt number on the heated plate is considered for the GCI analysis and is calculated with the jet total temperature ($T_{0\,\mathrm{jet}} = 298.2\,\mathrm{K}$) as the reference temperature (T_{ref}). The median GCI for the Nusselt number is about 4%. The simulations are considered to be converged where the mass flow rate fluctuations obtained at the outlet are in the order of 10^{-7}. Overall, the errors obtained are considered acceptable within the scope of the current study.

Large Eddy Simulation

Fig. 7 shows the computational domain for the LES, which does not consider the large plenum but begins at the entry plane of the 9 jet holes. The arrows indicate the flow direction at the inflow and outflow boundaries. The inflow conditions for each jet hole are extracted from preliminary RANS computations of the configuration including the plenum to be able to account for the non-homogeneous velocity distribution. They are prescribed as temporally constant 2D distributions using local Riemann boundary conditions. The solid wall boundaries are treated in the same manner as in the RANS simulations. At the outflow, a 1D non-reflecting boundary condition based on a characteristics formulation (Schlüß et al., 2016) controls the time-averaged pressure, which was determined iteratively to yield the required mass flow.

As discussed by Morsbach & Bergmann (2020), the TRACE finite volume method can be used to solve the filtered compressible Navier-Stokes equations using a second-order accurate, density based scheme applying MUSCL reconstruction with $\kappa = 1/3$ (van Leer, 1979) for the convective fluxes. A fraction of 10^{-3} of Roe's numerical flux (Roe, 1981) is added to a central flux to avoid odd-even decoupling. The viscous fluxes are computed using central differences. Time integration is performed using a third-order accurate explicit Runge-Kutta method. The subgrid stresses are computed using the WALE model of Nicoud & Ducros (1999).

The domain is meshed in a block-structured topology resulting in a total of $66.9 \cdot 10^6$ cells. The average non-dimensional cell sizes of the the wall adjacent cells are in line with recommendations for LES (Georgiadis et al., 2010) while the average values are well below these guidelines. The grid resolution was confirmed to be adequate by comparing the spatial cut-off scale and the estimated Kolmogorov length scale $\Delta_{\mathrm{cut}}/l_\eta = V^{1/3}/\left(\nu^3/\epsilon\right)^{1/4}$ (Fröhlich et al., 2005). More details on the mesh are given by Tabassum et al. (2022).

For unsteady analysis, data were sampled as summarised in Tab. 2 and Fig. 7. The probes represent structured datasets of primary variables and their gradients with dimensions as specified in the legend of Fig. 7. The focus was chosen to be on jet No. 7, which is why this region is the most densely sampled one. However, time series for any region of interest can be obtained from the full 3D data set sampled at a slightly lower frequency but at full spatial resolution using TRACE's ParaView Catalyst interface (Ayachit et al., 2015) and have also been used in the following analyses depending on the question if higher temporal or spatial resolution was required.

Table 2. Summary of data sampled from LES.

	Probes	Full 3D
Sampling rate / kHz	13.3	5.3
Sample length / s	0.69	0.619
Sample length / T_{ref}	136.8	122.7
Sample size / GB	106	7500

4. Results

4.1. Flow conditions

Using the orifice plate measurement, the mass flow rate at the channel outlet is adjusted to $\dot{m} = 20\,\mathrm{g/s}$ which results in an average exit Reynolds number of $\mathrm{Re}_D = 10\,000$ for each of the 9 jets with a bulk velocity of $U_{\mathrm{jet}} \approx 10\,\mathrm{m/s}$. For the iTSP measurements the heating was achieved using carbon nano tube heating layer which was supplied with currents of $I = 3{-}7\,\mathrm{A}$ at voltages of $80{-}120\,\mathrm{V}$ to achieve a heat fluxes in the range of $2{-}5\,\mathrm{kW/m^2}$. With a constant mass flow rate of $\dot{m} = 20\,\mathrm{g/s}$ the heating block (i.e. target plate) reaches steady state temperatures of $T_{\mathrm{bulk}} = 37{-}56^{\circ}\mathrm{C}$. Due to the placement of the heating layer close to the surface of the plate, thermal boundary conditions similar to the conditions found in the LES, where most of the energy is transported into the flow, are achieved.

4.2. The global flow field

The flow field is characterised with both conventional (snap-shot) PIV to provide overview data as well as TR-PIV at higher image magnifications to focus on particular areas of interest. A condensed version of the PIV data base is given in Table 1.

Figure 9, top, shows the mean normalized velocity along the channel's center plane ($y = 0$). The streamlines further highlight the mean flow topology with jet roll-up structures clearly visible in the jet impingement areas. A detailed comparison of the mean flow field with results obtained by both RANS and LES is provided by Tabassum et al. (2022).

4.3. Flow dynamics around jet No. 7

In order to study the interaction of a single jet with its surroundings and possibly uncover inter-jet dynamics the domain around jet No. 7 is singled out for detailed measurements. The flow of jet No. 7 can be considered more or less converged with respect to its neighbors, jet No. 6 and jet No. 8, while at the same time not yet being affected by the outflow (cf. Figure 8). Also, the cross-flow around jet No. 7 is not yet strong enough to induce a complete detachment of the jet's streamline.

Using PIV the near-wall flow below jet No. 7 is captured at different image magnifications, sampling rates and light-sheet orientations. An overview of the near-wall flow is given in Fig. 10, showing streamlines compiled from three separately sampled ROIs. Near-wall profiles of streamwise velocity and variances at center-plane are shown in Fig. 11. Due to its high spatial resolution, the acquired data allows for an accurate characterization of the turbulent boundary layer (TBL) developing downstream of the jet's impingement area (wall-jet region) and indicates a self-similar behavior when normalized with the local peak velocity (U_{max}) and boundary layer thickness, δ_{99}. The (unsteady) wall shear stress can be estimated using the velocity gradient at the wall. This in

turn gives access to shearing velocity u_τ and allows estimation of the local viscous scales (Willert, 2015) which are summarized in Table 3.

The boundary layer below the wall jet is very similar to a classical TBL subjected to an adverse pressure gradient (APG) due to its deceleration as it progresses away from the stagnation point. This spatial variation is also reflected in the shape factor H starting from $H = 1.40$ at $x/D = 1.33$ and increasing to $H = 2.33$ at $x/D = 4.66$ which indicates a trend toward relaminarization. For reference, $H = 2.59$ for a laminar (Blasius) boundary layer and $1.3 < H < 1.4$ for a zero pressure gradient (ZPG) TBL. Correspondingly, the viscous scales also increase from a minimum of $\nu/u_\tau = 27$ µm at $x/D = 2.0$ to $\nu/u_\tau = 49$ µm at $x/D = 4.66$. Near the stagnation point the estimation of the boundary layer quantities is less reliable as the mean velocity approaches zero. At $x/D = 1.33$ the viscous scale is actually larger than at $x/D = 2.00$ because the friction velocity also decreases when approaching the stagnation point. The adequate description of the near-wall flow in regions close to the stagnation point involves more complex formulations, taking into account the local pressure gradient, such as those proposed by Nickels (2004) and Knopp et al. (2020).

Table 3. Characteristics of the TBL downstream of jet No. 7.

Position	x/D	1.33	2.00	2.66	3.33	4.00	4.66	
BL thickness	δ_{99}	0.63	0.72	0.93	1.10	1.43	1.63	[mm]
displacement thickness	δ_1	0.34	1.08	1.09	0.96	0.87	0.46	[mm]
momentum thickness	δ_2	0.24	0.72	0.70	0.61	0.54	0.20	[mm]
shape factor	$H = \delta_1/\delta_2$	1.40	1.50	1.56	1.57	1.61	2.33	
friction velocity	u_τ	0.46	0.56	0.51	0.46	0.40	0.31	[m/s]
viscous scale	ν/u_τ	33	27	30	33	38	49	[µm]

4.3.1. Near-wall motions

The flow near the target plate, in particular in the stagnation zones of the jets is dominated by both downward motions, bringing cool fluid toward the warm target plate, as well as upward motions, removing warmer (spent) fluid from the plate. The latter is also referred to as “fountain flow" or ejections. These motions can be readily captured with 2D-2C flow field measurements in a plane close to the wall as outlined in Fig. 12. Under the assumption of incompressibility, $\nabla \mathbf{u} = 0$, the quantity

$$\nabla_{xy} = \frac{\partial u}{\partial x} + \frac{\partial v}{\partial y} = -\frac{\partial w}{\partial z} \tag{1}$$

can be estimated from the PIV data and provides 2D distributions of the regions of down-wash and up-welling.

The quantity ∇_{xy} is estimated from the TR-PIV data obtained in the wall-parallel xy-plane about 1 mm above the target plate using finite differences on the velocity components u, v. Mean and rms of ∇_{xy} are given in Fig. 13 a,b. Sub-figures 13 c,d and 13 e,f respectively show conditional averages

highlighting stronger impingement and ejection events, with 3 and 6 standard deviations away from the global mean. The strongest impingement events and overall magnitude coincides with stagnation point (line) of the jet at about $x/D = 1$. For jet No. 7 the area of strongest ejections, removing warm fluid from the surface, is located right below the jet at $x/D \approx 0.2$. This position coincides with the “hot-spot" on the target surface; it receives the least amount of fresh air from the impinging jet. A small fraction of stronger ejection events ($\approx 10\%$) are also present within the area of the wall jet from $x/D = 1$ onward.

Figure 14 provides a compilation of various quantities obtained along the centerline ($y = 0$) on the target plane (temperature) or slightly above it (velocity). The predicted Nusselt number distribution shows discrepancies in particular near the peaks with RANS providing higher values compared to LES. Measurements of the temperature distribution from TSP are not available for comparison due to the low signal levels (see Sect. 2.2). The side-by-side comparison of various velocity-based quantities nonetheless suggests that the Nusselt number distribution can be qualitatively predicted using measured flow field data. In particular, two quantities nearly follow the Nusselt distribution: (1) the square root of the sum of velocity variances, that is, the square root of the turbulent kinetic energy, and (2) the square root of the in-plane velocity divergence ∇_{xy}. The agreement with the first quantity indicates that high turbulence leads to high mixing and thus higher heat transfer. High values of the in-plane velocity divergence of the wall-parallel velocity components are associated with bursts of impingement flow that additionally lead to a renewal of the thermal boundary layer and hence an increased heat transfer. The iTSP data further indicate that the highest temperature fluctuations coincide with the regions of highest turbulence and peak heat transfer.

A qualitative comparison between the numerically predicted two-dimensional Nusselt number distribution and the measured quantities is given in Fig. 15. In spite of the limited ROI, of good agreement between Nusselt distribution and both the turbulence distribution and the fluctuation of the in-plane divergence can be observed. It should be noted that this turbulence-based quantity lacks the out-of-plane component $\langle w'w' \rangle$. A stereoscopic PIV measurement of the near-wall flow would be required to complement this empirical heat transfer distribution.

4.3.2. Velocity spectra

The time-resolved nature of the TR-PIV also enables the calculation of velocity power spectra. Here, Fig. 16 presents spectra for selected locations within the impingement area of jet No. 7 at four points as indicated in Fig. 10. For the TR-PIV data a 2$^{\text{nd}}$ order Butterworth lowpass filter with cut-off at 8 kHz removed the high frequency noise content in the TR-PIV data which is responsible for the change in energy decay rate beyond $f \approx 5\,\text{kHz}$. Noteworthy is that none of the spectra exhibit a dominant frequency that could be related to vortex shedding or periodic convection of dominant large scale flow structures. Rather, the spectra are nearly representative of the classical turbulence energy cascade including a K-5/3 energy decay rate as predicted by turbulence theory.

In the wall jet ($x/D > 1.5$) the K-5/3 decay spans a range of about 1 decade for the streamwise component u (100 – 2 000 Hz), whereas the wall-normal component w shows a continuous roll-off throughout with increasing frequencies, a clear indication of the non-isotropic nature of the wall jet. This finding is confirmed by the sampled LES data, as shown in Fig. 16 b for the same points close to the wall. As the wall jet develops, it decelerates (loses energy) with increased dissipation visible in the spectra, in particular at $x/D = 4$.

4.3.3. Autocorrelation and integral scales

Per definition the integral time scale T_u (or length scale L_u) of a quantity $u(\mathrm{x}, t)$ can be calculated from the autocorrelation function R_{uu} for a given quantity u:

$$R_{u_i u_i}(\tau) = \frac{\langle u_i(t)\, u_i(t+\tau)\rangle}{\sigma_{u_i}\, \sigma_{u_i}} \tag{2}$$

yielding the integral time scale through integration of R_{uu} from zero to infinity (Pope, 2000; George, 2013):

$$T_x = \int_{\tau=0}^{\infty} R_{uu}(\tau)\, d\tau \tag{3}$$

Of course, the infinite time delay obviously cannot be fulfilled for data obtained from experiments. Given the limited temporal and spatial domain of the measurements and LES calculations, the upper limit of integration is chosen to coincide with the first zero crossing of the autocorrelation signal. Estimates of the integral time scales as obtained from the TR-PIV measurements in the xz-plane at midspan and in the xy-plane 1 mm above the target plate are respectively plotted in Fig. 17. Time is normalized by the reference time $t_{\mathrm{ref}} = D/U_{\mathrm{jet}} = 1.21$ ms. The measure of anisotropy T_{xy} is defined as follows:

$$T_{xy} = \begin{cases} T_x/T_y - 1 & \text{if } T_x > T_y, \\ 0 & \text{if } T_x = T_y, \\ 1 - T_y/T_x & \text{if } T_x < T_y. \end{cases} \tag{4}$$

Regions of nearly isotropic turbulent flow with $T_{xz} \approx 0$ are present above the wall between the jets whereas the jet core flow and near-wall flow, e.g. wall jet, exhibits significant anisotropy with the time-scale of the streamwise velocity T_x more than 5 times higher than for the wall-normal velocity T_z. This agrees with the strong differences observed between the spectra of u and w. In the wall-parallel xy-plane the anisotropy T_{xy} between the streamwise and spanwise time-scales is not as pronounced, in particular, in the areas between the jets where the boundary layers below the wall jet form.

4.3.4. Two-point correlations

Two-point correlations provide a measure of similarity between the data u_1 at a given point $\mathbf{x}_0$ in space $\mathbf{x}$ (or time) with respect to the data u_2 in its neighborhood and is calculated from the snap-shot data $u_i = u_i\,(x, y, z, t)$ using the discrete version of the cross-correlation coefficient:

$$R_{u_i u_j}(\mathbf{x}, \mathbf{x}_0) = \frac{\int u_i'(\mathbf{x}, t)\, u_j'(\mathbf{x}_0, t)\, dt}{\sqrt{\int u_i'(\mathbf{x}, t)\, u_i'(\mathbf{x}, t)\, dt} \cdot \sqrt{\int u_j'(\mathbf{x}_0, t)\, u_j'(\mathbf{x}_0, t)\, dt}} \tag{5}$$

$$= \frac{\langle u_i'(\mathbf{x}, t) \cdot u_j'(\mathbf{x}_0, t) \rangle}{\sigma_{u_i}(\mathbf{x}) \cdot \sigma_{u_j}(\mathbf{x}_0)} \tag{6}$$

where $\sigma_{u_j}(\mathbf{x}_i)$ is the square root of the variance of all samples u_j at the point $\mathbf{x}_i$.

Two-point correlations are calculated for two distinct positions in the flow field, one on the center streamline of the jet at $z/D = 1$ and the other within the wall-jet at $x/D =$ -1.5. Correlation maps for the LES data are given in Fig. 18 for all available velocity component combinations. Although the flow is not homogeneous in the y-direction, the two-point correlation has been performed for the planes $y/D =$ {-0.2, -0.1, 0.0, 0.1, 0.2} independently and averaged to reduce the small scale noise. Fig. 19 provides similar maps for the snapshot based PIV data using 3 000 samples (120 s) but only for 4 of 9 possible correlation terms. While the limited simulation length of the LES results in noisier correlation maps, there is consistency between simulation and experiment both in terms of spatial extent and amplitude, for instance, for R_{UU} and R_{WW} at both sample locations. This permits the observation of possible correlations not accessible through the experiment. In this sense, R_{VW} indicates that spanwise motions in the jet (v') seem to have a significant influence on the vertical component w' as far as the following downstream jet. Also, R_{UW} indicates that axial motions of the jet (u') have an influence on w' in a large domain.

Switching to the wall jet, the correlation maps only show smaller regions of significant correlation. Of relevance here is the observation that coherent motions within the turbulent flow of the wall jet essentially leave no imprint on the jet impingement zone immediately downstream.

A more detailed view of the spatial correlations is provided in Fig. 20 using the high-magnification TR-PIV data in the central xz-plane and the xy-plane parallel to the surface. Here, modulations of the streamwise velocity have a very limited influence on the wall-jet itself, but have a wide footprint in spanwise direction indicating the impingement of large scale, coherent structures on the target plate. The spanwise modulation at the stagnation point ($x/D = 0.9$, $y/D = 0$) has a much wider signature in streamwise direction and could be related to the spanwise motion of the wall jet itself. This is also seen in visualizations of the wall-parallel flow. The only quantity with a noteworthy signature beyond the jet spacing is the correlation between streamwise and spanwise velocity R_{uv}.

As the presented two-point correlations are based on snapshot data, they do not provide information regarding possibly temporally delayed interactions. While not presented herein, space-time

correlations were calculated from the TR-PIV data but did not reveal a delayed response of the impinging jet to an upstream disturbance of the approaching wall jet.

4.3.5. Modal analysis

The spatially and temporally resolved data from both the LES as well as TR-PIV measurements lend themselves for the investigation of spatio-temporal inter-dependencies of the jets with the target plate and to retrieve the large scale dynamics of the flow. Suitable analysis methods include proper orthogonal decomposition (POD), also known as principal component analysis (PCA), dynamic mode decomposition (DMD) (Schmid, 2011) and spectral proper orthogonal decomposition (SPOD) (Towne et al., 2018; Schmidt & Colonius, 2020).

To perform the modal decomposition RPCA Candès et al. (2011) was initially chosen in order to separate noise from the raw measurement data by decomposing the data matrix into a low rank matrix and a sparse matrix, the latter of which containing the noise. However, this was found to bring no improvement over applying standard PCA (e.g. POD) on the unconditioned data. When separated into the respective matrices the variance of sparse matrix was 5 orders of magnitude lower than the low rank matrix. The distributions of modal contributions (e.g. Fig. 21) was not affected. A minor influence could be observed by temporally filtering the velocity data at a cutoff frequency of 5 kHz (see Fig. 25)

Figure 21 provides the relative and cumulative energy distributions of the velocity components u, w in the xz-plane computed from 3 000 snapshots recorded at 25 Hz. The first 100 modes of the velocity field contribute 60 – 70% of the energy, whereas the energy is much more distributed for the vorticity field ω_y with the first 100 modes making up only one third of the total energy.

The 10 most energetic POD modes are plotted in Fig. 22. Noteworthy is the presence of coherent structures in the streamwise component u along the jets' trajectories for Mode 4 and higher. The structures have spatial wavelengths comparable to the jet diameter and appear about $2\,D$ from the wall. Similar structures are also present in the 2-point correlation data such as R_{uu} in Fig. 19 a. Concentrated vorticity with similar scale appear for mode 8 and higher. The more energetic vorticity modes (1–7) capture the jets' shear layers. The wall jet itself has practically no contribution in the first 10 modes.

POD was also performed on the wall shear stress vector (τ_x, τ_y) and temperature θ available through LES. In this case, the first 100 modes contain 50% of the contribution of the wall shear stress and 75% of the temperature fluctuations (Fig. 23).

The spatial modes of the shear stress vector (Fig. 24) are restricted to the impingement areas with little differences of the structure from one mode to the next, which is a manifestation of the random nature of the impingement process. On the other hand the temperature modes have a much larger footprint with the most energetic modes being crescent shaped similar to the Nusselt number distribution (cf. Fig. 15) or the unsteady temperature distribution (cf. Fig. 6).

4.3.6. Spectral mode analysis

Another variant of singular value decomposition (SVD) is SPOD that extends the classical snapshot based decomposition to include the temporal coherency of the data (Towne et al., 2018; Schmidt & Colonius, 2020). SPOD processing was performed using the Python packages *pySPOD* (Mengaldo & Maulik, 2021) or *spod_python* (Burrows, 2020).

Similar to the spectra shown in Figs. 16 the SPOD spectral density shows no dominant frequency content. Within the developing shear layer of the jet, however, dominant frequencies can be seen in Fig. 27 b) with the modes at 365 Hz and 612 Hz in Fig. 29 clearly corresponding to vortex shedding. It is interesting to note that the larger structures of the SPOD modes at 117 Hz do not originate at the jet orifice but rather manifest themselves only in the lower part of the domain. Comparing these high frequency modes with the SPOD analysis of the temperature at the wall (see Fig. 27 b and Fig. 30), it can be stated that there is no clear connection to wall heat transfer. Near the wall, these frequencies are only a part of a turbulent spectrum with no clear separation between the modes. However, there is a significant gap in mode energy between the first two modes in both the temperature and the velocity spectrum at lower frequencies between 10 Hz and 30 Hz. This is consistent with the SPOD spectra for the velocity data given in Fig. 26. The temperature SPOD modes at these lower frequencies are shown in Fig. 30 and show great similarity with the most energetic temperature POD modes provided in Fig. 24. They represent a large scale motion of the jet footprint at the wall resulting in significant temperature variations. Furthermore, the movement of the two adjacent jets is correlated in a complex manner as can be seen in both the temperature modes and the modes for the wall shear stress vector. This large scale motion can also be found in the first velocity SPOD mode at 13 Hz, which can be interpreted as variation of the jet trajectory within the (xz)-plane.

5. Discussion and concluding remarks

Among the most prevalent findings in this study is the observation that none of the applied data post-processing methods (e.g. 2-point correlation, spatio-temporal correlation, POD, SPOD) reveal a direct interaction of an individual jet with its immediate neighbors. This indicates that the jets – at least near the downstream end – dominate their immediate surroundings and are only influenced by the global bulk flow that impose a deflection of the jet streamline toward the exit. At the same time the jets' interaction with the target plate is purely stochastic, showing no dominant frequencies in either time or space. Some dominant frequency content could be observed in the LES (Fig. 27 b) but could potentially be attributed to the roughly $10\times$ shorter simulation time (0.62 s) in comparison to the total record length of the PIV measurements ($3\times$ 2.94 s).

The presence of the rigid side walls on both sides of the jet limits the spanwise motion of the jets. The more unconfined configuration of a 2D jet array configuration will most likely exhibit a more pronounced and maybe even synchronized (periodic) meandering of the jets.

The Nusselt number distribution on the target correlates very well with the square root of sum of the velocity variances and the square root of the variance of the in-plane divergence. This offers a possibility to evaluate heat transfer on a difficult topology prohibiting other heat transfer measurement methods – especially if these interpretations are supported by additional (point-wise) thermal measurements.

Small scale structures in the wall jet are visible, these appear to fluctuate randomly and form cold fronts and streaks propagating in downstream direction along the target plate. These structures seem to be linked to the vortex shedding in the shear layers of the jet. The sudden fluid acceleration causes surface renewal- and turbulent mixing effects, beneficial for the heat transfer. If these effects can be manipulated and further enforced by geometric features, this could lead to enhanced heat transfer.

The first four modes of the (random) movement of the jets contain $\approx 20\%$ of the energy, however no clear prevalence of these four modes is recognizable. The movement of the jets "widens" the effective stagnation zone and thus increases the (time-averaged) area with high heat transfer. The frequency of these movements is around 10x smaller compared to the frequency of the vortex shedding. It remains unclear what triggers this large scale movement. This movement of the jets is a mechanism that should be further explored in order to maximize heat transfer and to reduce hot spot effects. In future work, geometric features in the impingement hole, on the impingement or target plate could be used to enhance (or damp) the meandering movement of the jets and thus improve the heat transfer.

Nomenclature

Af	relative nozzle area: $\frac{A_{\text{nozzle}}}{A_{\text{target}}}$
D	jet diameter [m]
H	separation distance [m]
p	pitch [m]
k	thermal conductivity [W/mK]
L	length [m]
Nu	Nusselt number: $\frac{q_{\text{wall}} D}{k_t (T_{\text{wall}} - T_{\text{ref}})}$
Pr	Prandtl number
q_w	specific wall heat flux W/m^2
Re_D	jet Reynolds number: $\frac{u_{\text{jet}} D}{\nu_{\text{jet}}}$
T	temperature [K]
T_0	total temperature [K]
U, V, W	mean velocity components [m/s]
u, v, w	velocity components [m/s]

u', v', w'	fluctuating velocity components [m/s]
W	width [m]
x, y, z	spatial coordinates [m]
$\Delta x_{\|\|}^+$	near-wall grid size (wall-parallel)
y_1^+	near-wall grid size (wall-normal)
θ	normalised temperature: $\frac{T - T_{\text{jet}}}{T_{\text{max}} - T_{\text{jet}}}$
ν	kinematic viscosity [m^2/s]
ω	vorticity [s^{-1}]
∇_{xy}	in-plane divergence [s^{-1}]

References

Amano, R., & Sundén, B. (2014). *Impingement jet cooling in gas turbines*. WIT Press.

Ayachit, U., Bauer, A., Geveci, B., O'Leary, P., Moreland, K., Fabian, N., & Mauldin, J. (2015). Paraview catalyst: Enabling in situ data analysis and visualization. In *proceedings of the first workshop on in situ infrastructures for enabling extreme-scale analysis and visualization*. New York, NY, USA: Association for Computing Machinery. DOI: 10.1145/2828612.2828624

Behn, M., Hilfer, M., Klein, C., Ahlefeldt, T., Enghardt, L., & Tapken, U. (2021). Validierung von Übertragungsmodellen für ortsfeste und rotierende Schallquellen in Strömungskanälen durch drucksensitive Farbe. In *DAGA 2021 - 47. Jahrestagung für Akustik.* Retrieved from `https://elib.dlr.de/145959/`

Brakmann, R., Chen, L., Weigand, B., & Crawford, M. (2016). Experimental and numerical heat transfer investigation of an impinging jet array on a target plate roughened by cubic micro pin fins. *Journal of Turbomachinery*, *138*(11). DOI: 10.1115/1.4033670

Burrows, T. J. (2020). *Python spod code.* `https://github.com/tjburrows/spod_python`. GitHub. Retrieved from `https://github.com/tjburrows/spod_python`

Candès, E. J., Li, X., Ma, Y., & Wright, J. (2011, jun). Robust principal component analysis? *J. ACM*, *58*(3). DOI: 10.1145/1970392.1970395

Dairay, T., Fortuné, V., Lamballais, E., & Brizzi, L.-E. (2015). Direct numerical simulation of a turbulent jet impinging on a heated wall. *Journal of Fluid Mechanics*, *764*, 362394. DOI: 10.1017/jfm.2014.715

Dewan, A., Dutta, R., & Srinivasan, B. (2012). Recent trends in computation of turbulent jet impingement heat transfer. *Heat Transfer Engineering*, *33*(4-5), 447–460. DOI: 10.1080/01457632.2012.614154

Dutta, S., & Singh, P. (2021). Opportunities in jet-impingement cooling for gas-turbine engines. *Energies*, *14*(20). DOI: 10.3390/en14206587

Fröhlich, J., Mellen, C. P., Rodi, W., Temmerman, L., & Leschziner, M. A. (2005). Highly resolved large-eddy simulation of separated flow in a channel with streamwise periodic constrictions. *Journal of Fluid Mechanics*, *526*, 1966. DOI: 10.1017/S0022112004002812

Gaffuri, M., Terzis, A., & Ott, P. (2019). Narrow impingement channels: recent advancements and future directions. *13th European Conference on Turbomachinery Fluid Dynamics and Thermodynamics*(ETC2019-252). Retrieved from `http://www.euroturbo.eu/paper/ETC2019-252.pdf`

Geiser, G., Wellner, J., Kügeler, E., Weber, A., & Moors, A. (2019, 01). On the Simulation and Spectral Analysis of Unsteady Turbulence and Transition Effects in a Multistage Low Pressure Turbine. *Journal of Turbomachinery*, *141*(5). (051012) DOI: 10.1115/1.4041820

George, W. (2013). *Lectures in turbulence for the 21st century.* online at *www.turbulence-online.com*. Retrieved from `http://www.turbulence-online.com`

Georgiadis, N. J., Rizzetta, D. P., & Fureby, C. (2010). Large-eddy simulation: Current capabilities, recommended practices, and future research. *AIAA Journal*, *48*(8), 1772-1784. DOI: 10.2514/1.J050232

Gößling, J., Ahlefeldt, T., & Hilfer, M. (2020). Experimental validation of unsteady pressure-sensitive paint for acoustic applications. *Experimental Thermal and Fluid Science*, *112*, 109915. DOI: 10.1016/j.expthermflusci.2019.109915

Hadziabdic, M., & Hanjalic, K. (2008). Vortical structures and heat transfer in a round impinging jet. *Journal of Fluid Mechanics*, *596*, 221260. DOI: 10.1017/S002211200700955X

Hall, J. W., & Ewing, D. (2004, oct). The development of the large-scale structures in round impinging jets exiting long pipes at two reynolds numbers. *Experiments in Fluids*, *38*(1), 50–58. DOI: 10.1007/s00348-004-0883-2

Hossain, J., Fernandez, E., Garrett, C., & Kapat, J. (2018). Flow and heat transfer analysis in a single row narrow impingement channel: Comparison of particle image velocimetry, large eddy simulation, and RANS to identify RANS limitations. *Journal of Turbomachinery*, *140*(3), 031010. DOI: 10.1115/1.4038711

Jambunathan, K., Lai, E., Moss, M., & Button, B. (1992). A review of heat transfer data for single circular jet impingement. *International Journal of Heat and Fluid Flow*, *13*(2), 106–115. DOI: 10.1016/0142-727x(92)90017-4

Kataoka, K., Suguro, M., Degawa, H., Maruo, K., & Mihata, I. (1987). The effect of surface renewal due to largescale eddies on jet impingement heat transfer. *International Journal of Heat and Mass Transfer*, *30*(3), 559-567. DOI: 10.1016/0017-9310(87)90270-5

Kato, M., & Launder, B. (1993, 01). The modelling of turbulent flow around stationary and vibrating square cylinders. *Proceedings of the 9th Symposium on Turbulent Shear Flows, Kyoto, Japan*.

Klein, C., Henne, U., Deisuke, Y., Ondruss, V., Beifuss, U., Hensch, A.-K., & Quest, J. (2017). Application of carbon nanotubes and temperature sensitive paint for the detection of boundary layer transition under cryogenic conditions. In *55th aiaa aerospace sciences meeting* (p. 0336). DOI: 10.2514/6.2017-0336

Knopp, T., Novara, M., Schanz, D., Geisler, R., Philipp, F., Schroll, M., ... Schröder, A. (2020). Modification of the SSG/LRR- $$\omega $$ RSM for turbulent boundary layers at adverse pressure gradient with separation using the new DLR VicToria experiment. In A. Dillmann, G. Heller, E. Krämer, C. Wagner, C. Tropea, & S. Jakirli (Eds.), *New Results in Numerical and Experimental Fluid Mechanics XII* (Vol. 142, pp. 80–89). Cham: Springer International Publishing. (Series Title: Notes on Numerical Fluid Mechanics and Multidisciplinary Design) DOI: 10.1007/978-3-030-25253-3_8

Langtry, R., & Menter, F. (2009, 12). Correlation-based transition modeling for unstructured parallelized computational fluid dynamics codes. *AIAA Journal*, *47*. DOI: 10.2514/1.42362

Liu, T., Sullivan, J. P., Asai, K., Klein, C., & Egami, Y. (2021). *Pressure and temperature sensitive paints - second edition* (W. Merzkirch, D. Rockwell, & C. Tropea, Eds.) (No. 2). Springer, Cham. (Softcover ISBN 978-3-030-68058-9 eBook ISBN 978-3-030-68056-5 Series ISSN 1613-222X Series E-ISSN 2197-9510) DOI: 10.1007/978-3-030-68056-5

Liu, X., Qin, C., Tang, Y., Zhao, K., Wang, P., Liu, Y., ... Peng, D. (2022). Resolving dynamic features of kilohertz pressure fluctuations using fast-responding pressure-sensitive paint: measurement of inclined jet impingement. *Experiments in Fluids*, *63*(72). DOI: 10.1007/s00348-022-03419-4

Lynch, K., & Scarano, F. (2013). A high-order time-accurate interrogation method for time-resolved PIV. *Measurement Science and Technology*, *24*(3), 035305. DOI: 10.1088/0957-0233/24/3/035305

Martin, H. (1977). Heat and mass transfer between impinging gas jets and solid surfaces. *Advances in Heat Transfer, Academic Press, New York, 13, pp. 160*.

Mengaldo, G., & Maulik, R. (2021). PySPOD: A Python package for spectral proper orthogonal decomposition (SPOD). *Journal of Open Source Software*, *6*(60), 2862. DOI: 10.21105/joss.02862

Menter, F., Kuntz, M., & Langtry, R. (2003, 01). Ten years of industrial experience with the SST turbulence model. *Heat and Mass Transfer*, *4*.

Morsbach, C., & Bergmann, M. (2020). Critical analysis of the numerical setup for the large-eddy simulation of the low-pressure turbine profile T106C. In M. García-Villalba, H. Kuerten, & M. V. Salvetti (Eds.), *Direct and large eddy simulation xii* (pp. 343–348). Cham: Springer International Publishing.

Nickels, T. B. (2004). Inner scaling for wall-bounded flows subject to large pressure gradients. *Journal of Fluid Mechanics*, *521*, 217239. DOI: 10.1017/S0022112004001788

Nicoud, F., & Ducros, F. (1999, 09). Subgrid-scale stress modelling based on the square of the velocity gradient tensor. *Flow Turbulence and Combustion*, *62*, 183-200. DOI: 10.1023/A:1009995426001

Penumadu, P. S., & Rao, A. G. (2017). Numerical investigations of heat transfer and pressure drop characteristics in multiple jet impingement system. *Applied Thermal Engineering*, *110*, 1511-1524. DOI: 10.1016/j.applthermaleng.2016.09.057

Pope, S. B. (2000). *Turbulent flows*. Cambridge Univ. Press, Cambridge, UK.

Raffel, M., Willert, C., Kähler, C., Scarano, F., Wereley, S., & Kompenhans, J. (2018). *Particle Image Velocimetry: A Practical Guide (3rd edition)*. Springer-Verlag Berlin Heidelberg. DOI: 10.1007/978-3-319-68852-7

Rao, G. A., Levy, Y., & Kitron-Belinkov, M. (2009). Heat transfer characteristics of a multiple jet impingement system. In *48th Israeli Aerospace Conference* (pp. 5–7).

Rao, Y., Chen, P., & Wan, C. (2016). Experimental and numerical investigation of impingement heat transfer on the surface with micro w-shaped ribs. *International Journal of Heat and Mass Transfer*, *93*, 683-694. DOI: 10.1016/j.ijheatmasstransfer.2015.10.022

Rizk, M. H., & Menon, S. (1988). Large-eddy simulations of axisymmetric excitation effects on a row of impinging jets. *Physics of Fluids*, *31*(7), 1892. DOI: 10.1063/1.866636

Roache, P. J. (1994, 09). Perspective: A method for uniform reporting of grid refinement studies. *Journal of Fluids Engineering*, *116*(3), 405-413. DOI: 10.1115/1.2910291

Roe, P. (1981). Approximate Riemann solvers, parameter vectors, and difference schemes. *Journal of Computational Physics*, *43*(2), 357-372. DOI: 10.1016/0021-9991(81)90128-5

Schlüß, D., Frey, C., & Ashcroft, G. (2016). Consistent non-reflecting boundary conditions for both steady and unsteady flow simulations in turbomachinery applications. In *ECCOMAS Congress 2016 VII European Congress on Computational Methods in Applied Sciences and Engineering, Crete Island, Greece*.

Schmid, P. J. (2011). Application of the dynamic mode decomposition to experimental data. *Experiments in Fluids*, *50*(4), 1123–1130. DOI: 10.1007/s00348-010-0911-3

Schmidt, O. T., & Colonius, T. (2020). Guide to spectral proper orthogonal decomposition. *AIAA Journal*, *58*(3), 1023–1033. DOI: 10.2514/1.J058809

Schramm, J. M., & Hilfer, M. (2020). Time response calibration of ultra-fast temperature sensitive paints for the application in high temperature hypersonic flows. In A. Dillmann, G. Heller, E. Krämer, C. Wagner, C. Tropea, & S. Jakirlić (Eds.), *New Results in Numerical and Experimental Fluid Mechanics XII* (pp. 143–152). Cham: Springer International Publishing. DOI: 10.1007/978-3-030-25253-3_14

Tabassum, S., Hilfer, M., Brakmann, R. G., Willert, C. M. C., Matha, M., & Schroll, M. (2022). Validation and assessment of computational fluid dynamic modeling of multi-jet impingement cooling with the experiments. In *ASME Turbo Expo 2022: Turbomachinery Technical Conference and Exposition* (Vol. Heat Transfer, p. 12). Rotterdam, The Netherlands: International Gas Turbine Institute.

Terzis, A. (2016, aug). On the correspondence between flow structures and convective heat transfer augmentation for multiple jet impingement. *Experiments in Fluids*, *57*(9). DOI: 10.1007/s00348-016-2232-7

Terzis, A., von Wolfersdorf, J., Weigand, B., & Ott, P. (2015). A method to visualise near wall fluid flow patterns using locally resolved heat transfer experiments. *Experimental Thermal and Fluid Science*, *60*, 223-230. DOI: 10.1016/j.expthermflusci.2014.09.009

Towne, A., Schmidt, O. T., & Colonius, T. (2018). Spectral proper orthogonal decomposition and its relationship to dynamic mode decomposition and resolvent analysis. *Journal of Fluid Mechanics*, *847*, 821–867. DOI: 10.1017/jfm.2018.283

Tummers, M. J., Jacobse, J., & Voorbrood, S. G. (2011). Turbulent flow in the near field of a round impinging jet. *International Journal of Heat and Mass Transfer*, *54*(23), 4939-4948. DOI: 10.1016/j.ijheatmasstransfer.2011.07.007

Uddin, N., Neumann, S. O., & Weigand, B. (2013). LES simulations of an impinging jet: On the origin of the second peak in the Nusselt number distribution. *International Journal of Heat and Mass Transfer*, *57*(1), 356-368. DOI: 10.1016/j.ijheatmasstransfer.2012.10.052

van Leer, B. (1979). Towards the ultimate conservative difference scheme. v. a second-order sequel to Godunov's method. *Journal of Computational Physics*, *32*(1), 101-136. DOI: 10.1016/0021-9991(79)90145-1

Viskanta, R. (1993). Heat transfer to impinging isothermal gas and flame jets. *Experimental Thermal and Fluid Science*, *6*(2), 111–134. DOI: 10.1016/0894-1777(93)90022-b

Weigand, B., & Spring, S. (2011). Multiple jet impingement - a review. *Heat Transfer Research, vol. 42, no. 2, pp. 101-142*.

Westerweel, J., & Scarano, F. (2005). Universal outlier detection for PIV data. *Experiments in Fluids*, *39*(6), 1096-1100. DOI: 10.1007/s00348-005-0016-6

Willert, C. E. (2015). High-speed particle image velocimetry for the efficient measurement of turbulence statistics. *Experiments in Fluids*, *56*(1). DOI: 10.1007/s00348-014-1892-4

Zuckerman, N., & Lior, N. (2006). Jet impingement heat transfer: Physics, correlations, and numerical modeling. In *Advances in heat transfer* (pp. 565–631). Elsevier. DOI: 10.1016/s0065-2717(06)39006-5

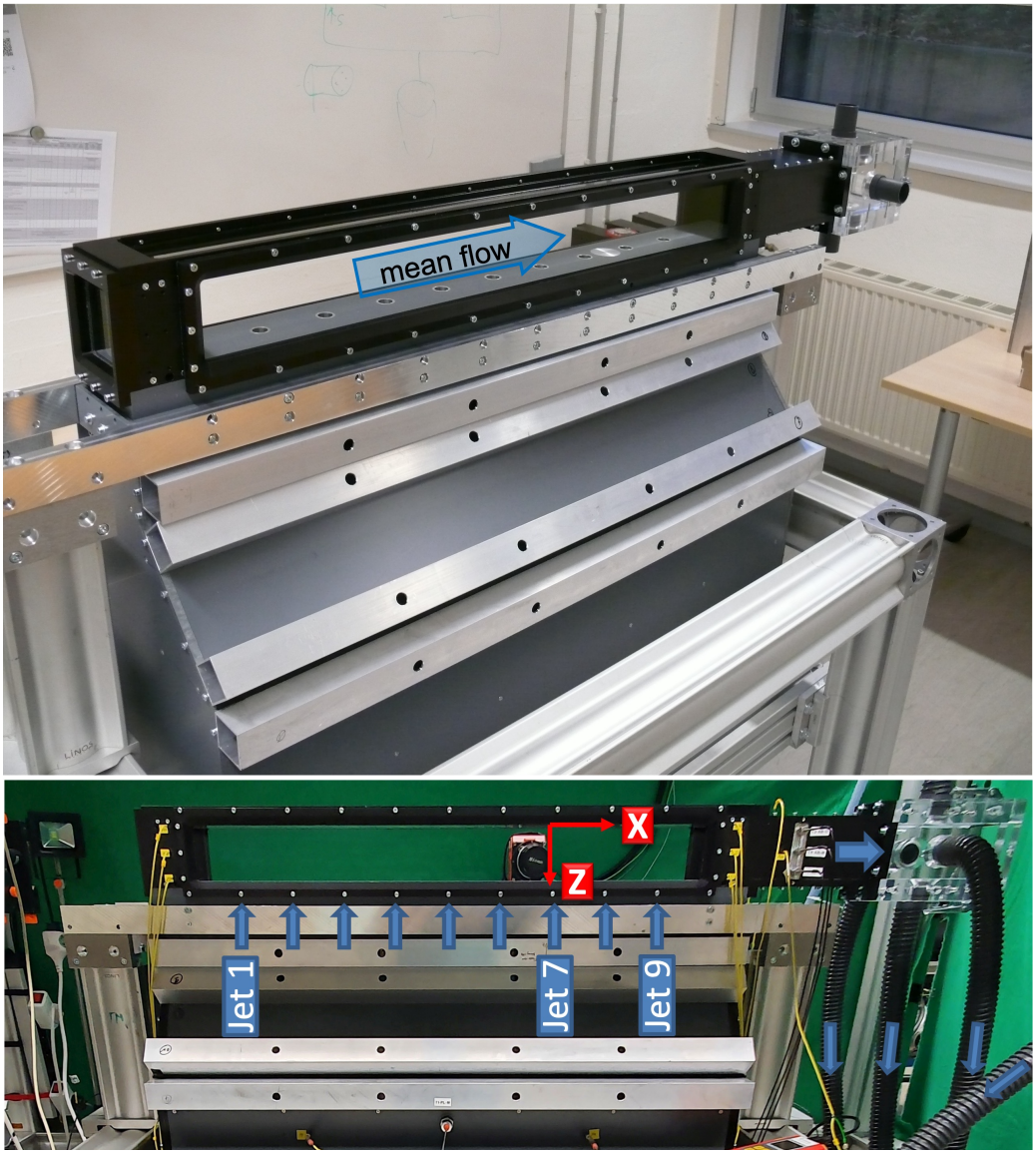

Figure 3. Top: jet impingement channel mounted on settling chamber with heated target plate removed and row of jet orifices clearly visible; bottom: completed laboratory installation of the cooling configuration. Note, that the plenum is at the bottom, the target plate is at the top.

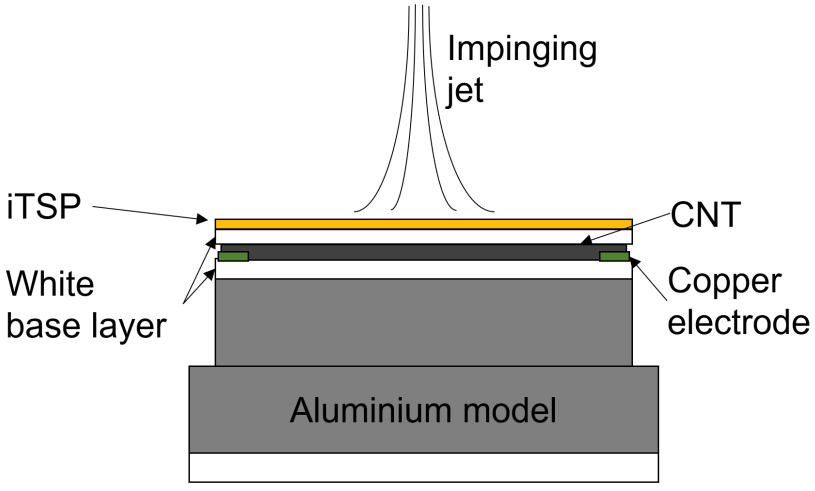

Figure 4. Sketch of the iTSP with incorporated heating CNT layer.

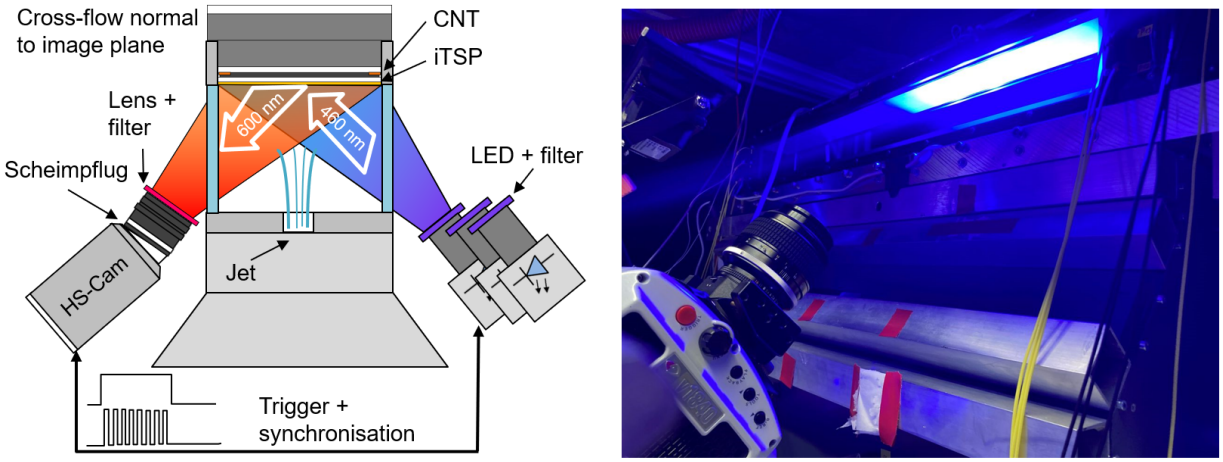

Figure 5. Sketch and photograph of the iTSP measurement setup: high-speed camera obliquely viewing the illuminated impingement area of jet No. 6 to jet No. 8. HP-LEDs are illuminating the area from the other side.

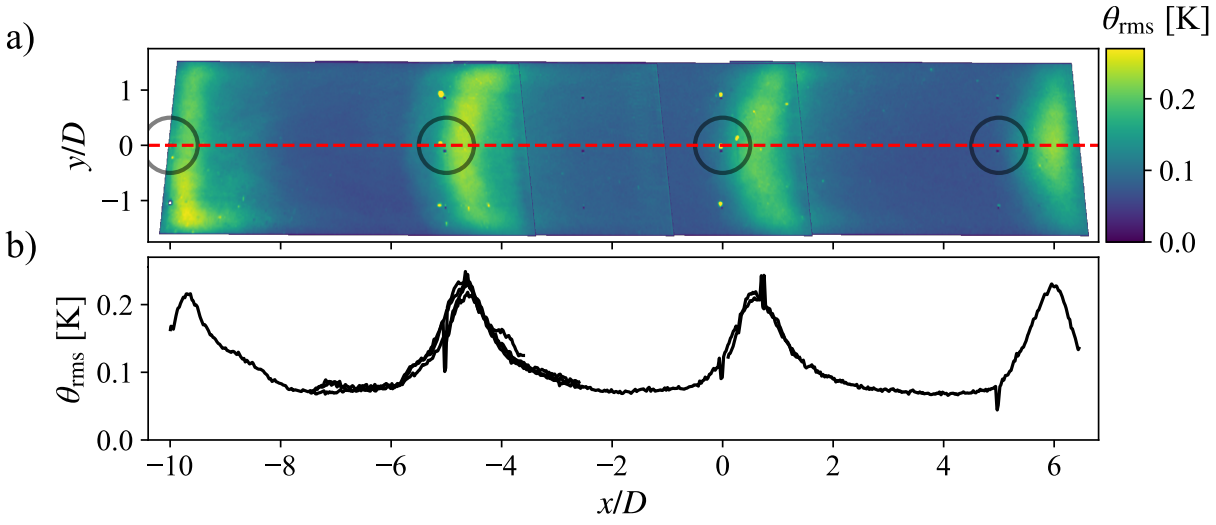

Figure 6. Distribution of the RMS temperature on the surface obtained from 5 separate iTSP measurements (**a**), RMS temperature profile along centerline ($y = 0$) as indicated by dashed red line (**b**). The spikes along the profiles are due to calibration markers on the target plate.

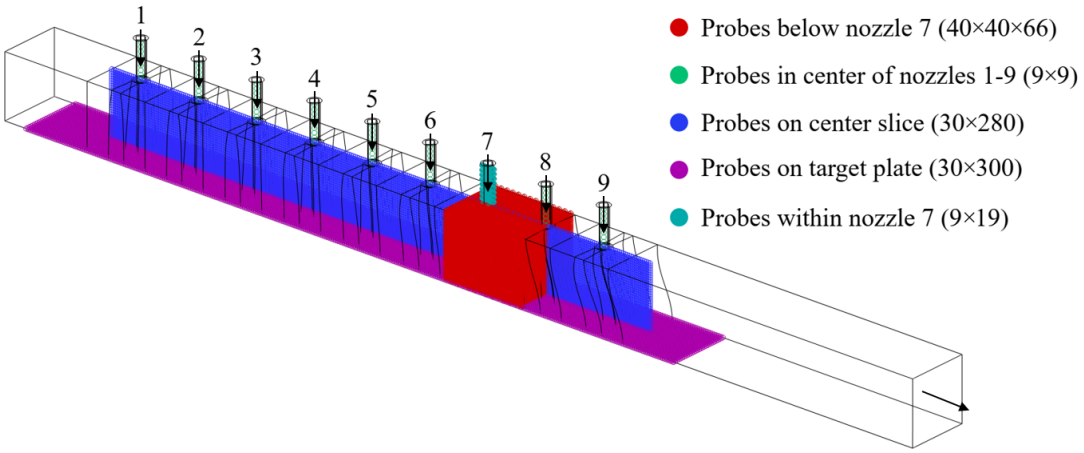

Figure 7. Computational domain of the LES including the probe positions at which data were sampled at high temporal resolution.

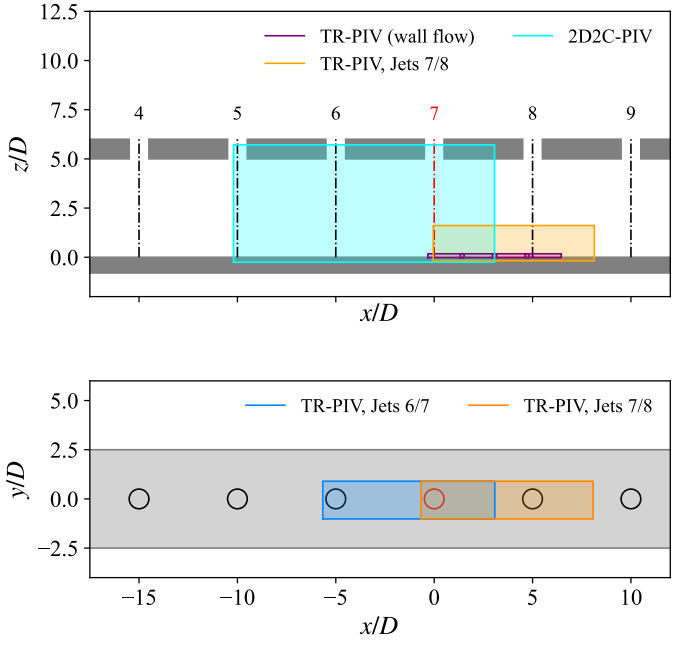

Figure 8. Measurement locations for PIV.

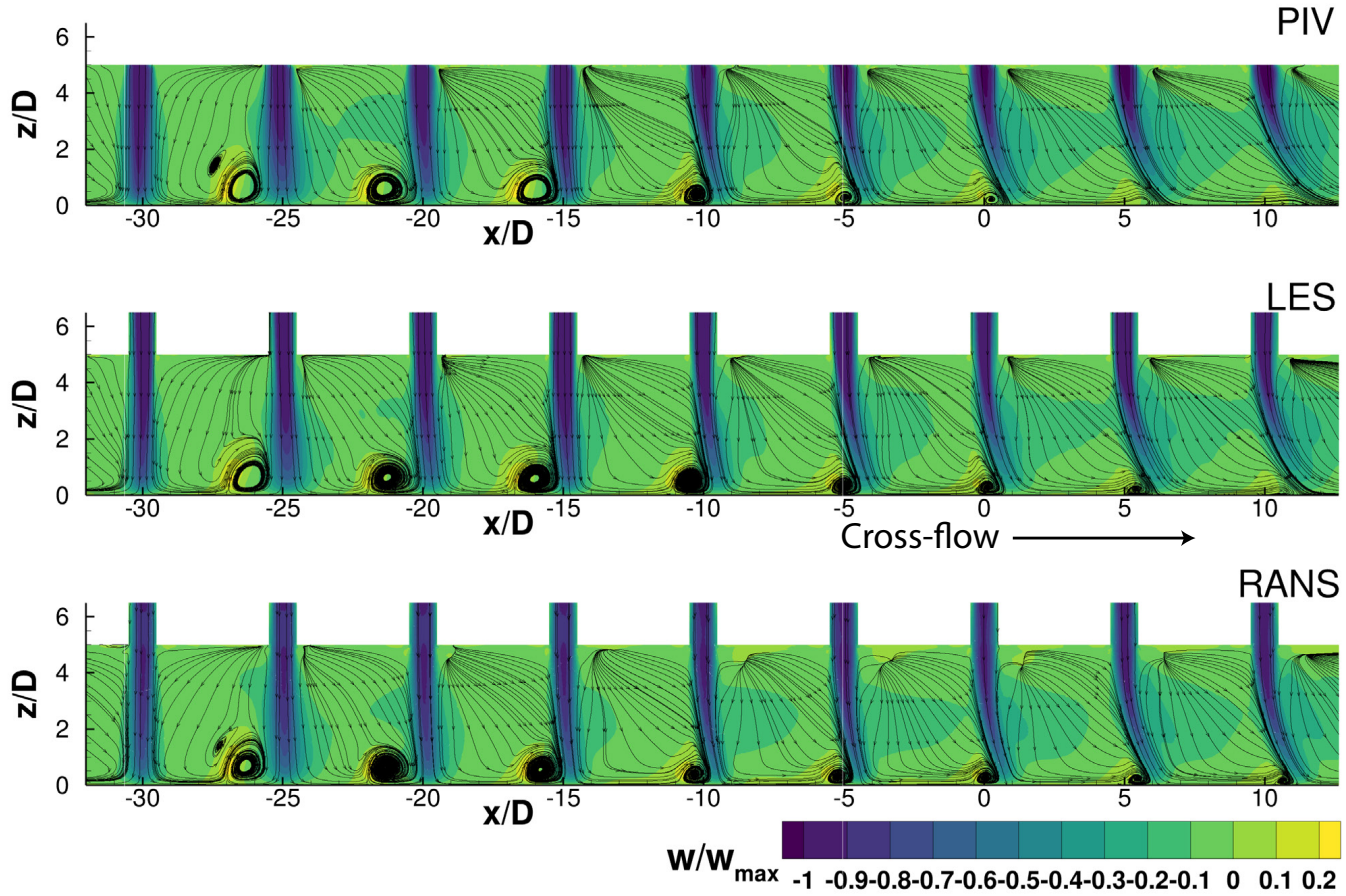

Figure 9. Mean velocity distribution in the center-plane ($y = 0$) obtained with PIV, LES and RANS normalized with respective jet No. 1 exit velocities of $W_{\mathrm{PIV}} = 12.60\,\mathrm{m/s}$, $W_{\mathrm{RANS}} = 15.24\,\mathrm{m/s}$ and $W_{\mathrm{LES}} = 15.06\,\mathrm{m/s}$.

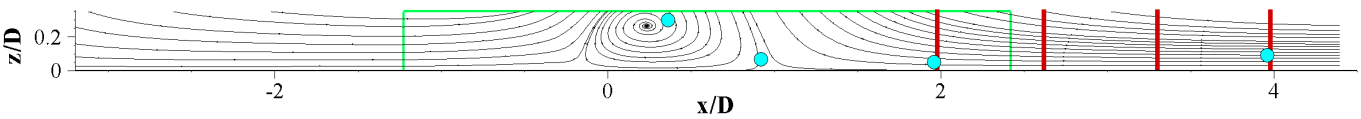

Figure 10. Streamlines of the mean near-wall velocity field at center-plane ($y = 0$) below jet No. 7 obtained by overlaying 3 high-magnification TR-PIV data sets. Vertical red lines at $x/D = 2.0, 2.6, 3.3, 4.0$ indicate sampling positions for velocity profiles; cyan dots indicate sample points for velocity spectra. Green box outlines size of TR-PIV sampling domain.

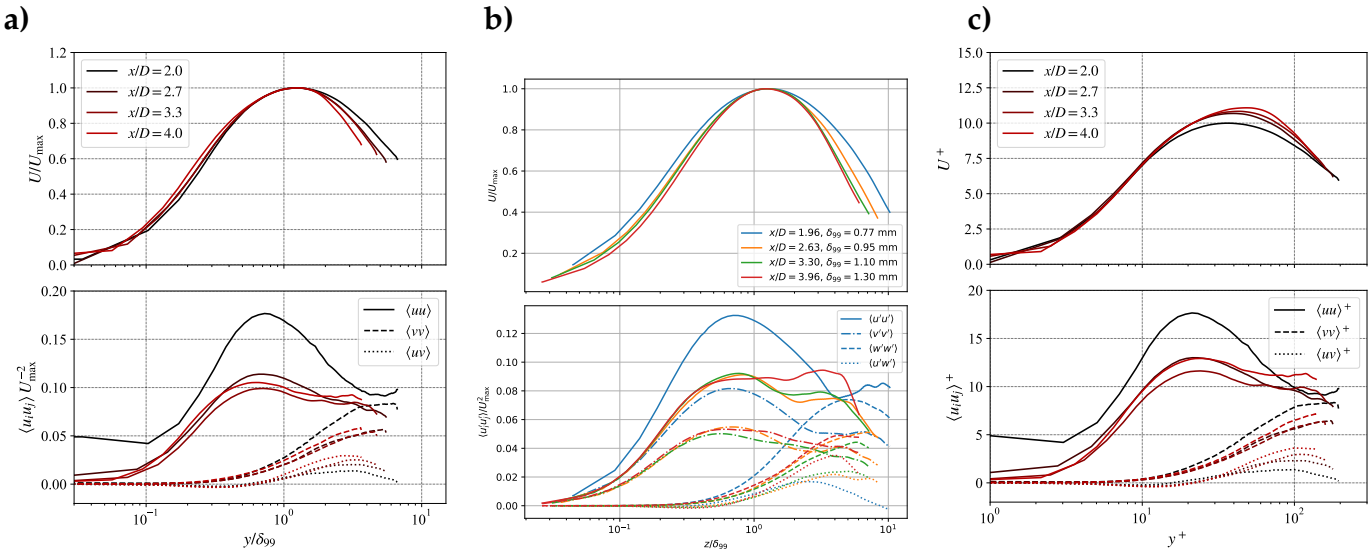

Figure 11. Near-wall profiles of streamwise velocity and variances at center-plane ($y = 0$) below jet No. 7 normalized with maximum velocity $U_{\max}$ and TBL thickness δ_{99} obtained with high-magnification TR-PIV (**a**) and LES (**b**). Profiles in viscous scaling (**c**) are based on characteristic parameters of the developing TBL as given in Table 3.

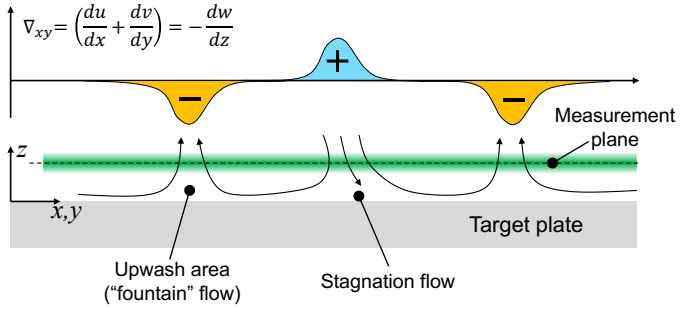

Figure 12. Schematic of the near-wall flow showing down-wash and up-welling motions. The horizontal green shaded line indicates a wall-parallel plane imaged by PIV.

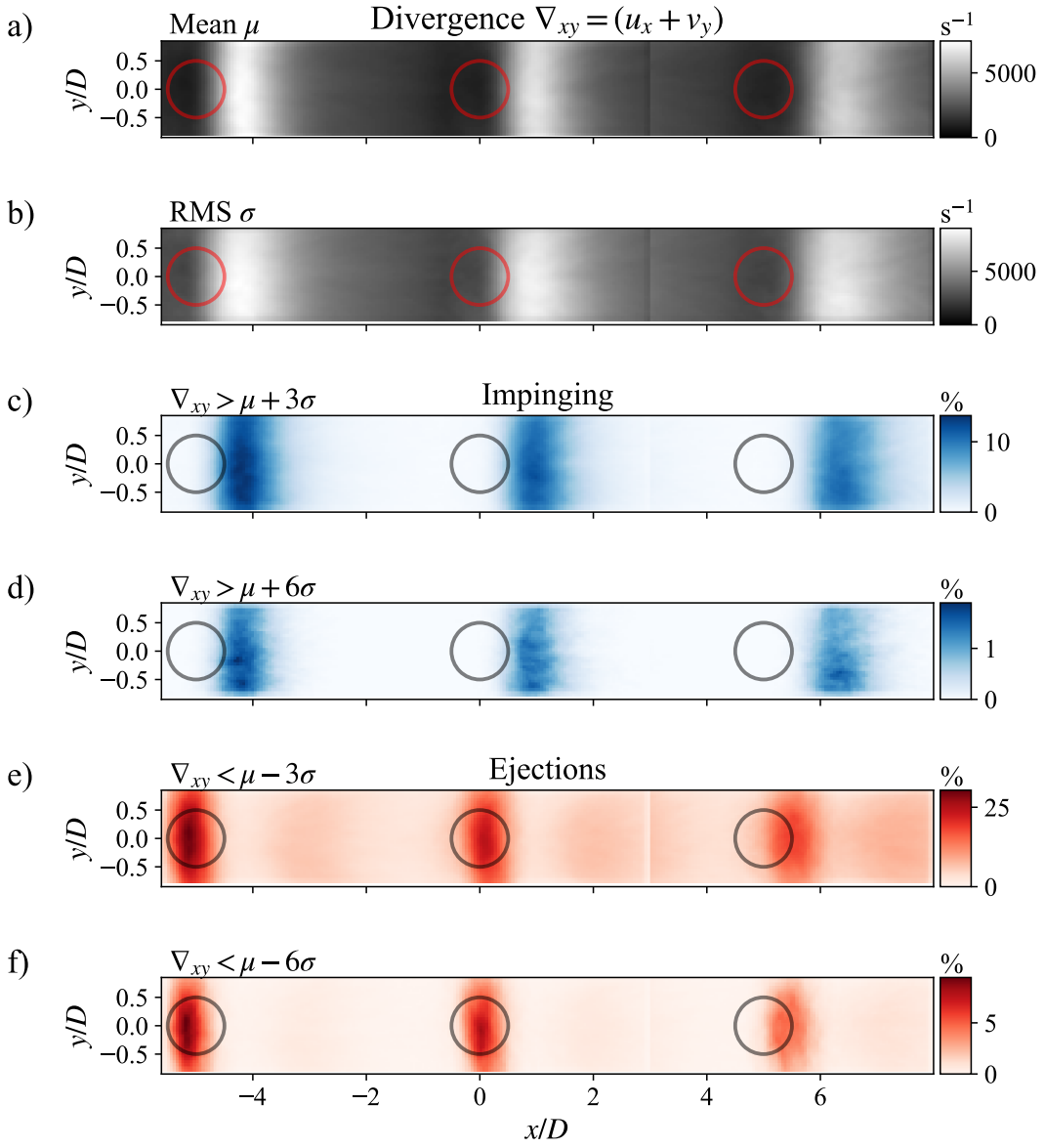

Figure 13. 2d distributions of the quantity ∇_{xy} about 1 mm from the target plate, mean (**a**) and standard deviation (**b**). Sub-figures (**c**) and (**d**) show percentage of down-wash events of $3\,\sigma$ and $6\,\sigma$ above the global mean. Sub-figures (**e**) and (**f**) show percentage of fountain flow events (ejections) of $3\,\sigma$ and $6\,\sigma$ below the global mean.

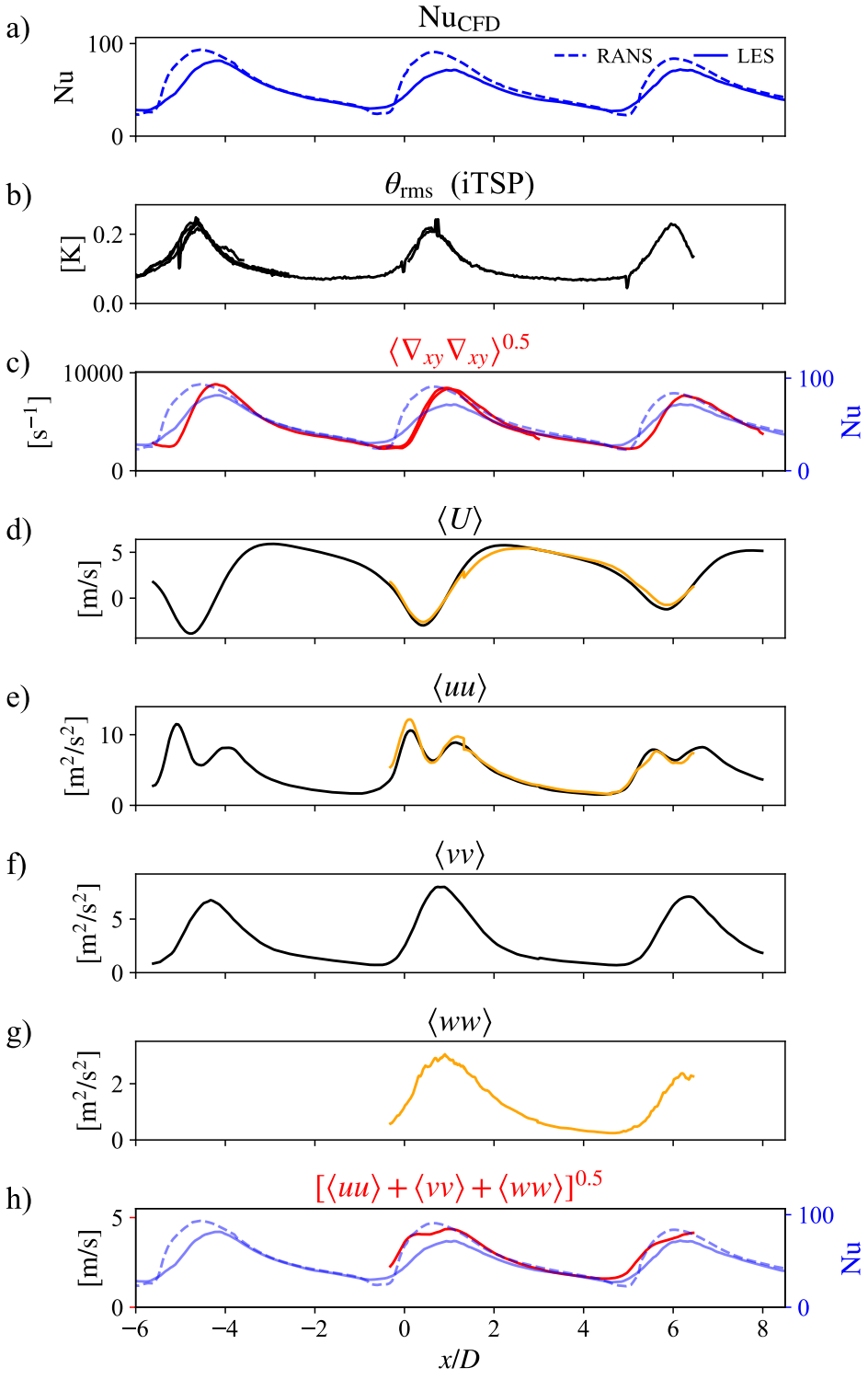

Figure 14. Nusselt number distribution at the centerline ($y = 0$) obtained with LES and RANS (**a**) compared with various measured quantities; standard deviation of temperature θ_{rms} from iTSP (**b**), standard deviation of ∇_{xy} (**c**), mean streamwise velocity u (**d**), velocity variances $\langle uu \rangle$ (**e**), $\langle vv \rangle$ (**f**) and $\langle ww \rangle$ (**g**). Black profiles from xy-plane; orange profiles from xz-plane. (**h**): Square root of sum of variances overlaid with Nusselt number distribution shown in (**a**).

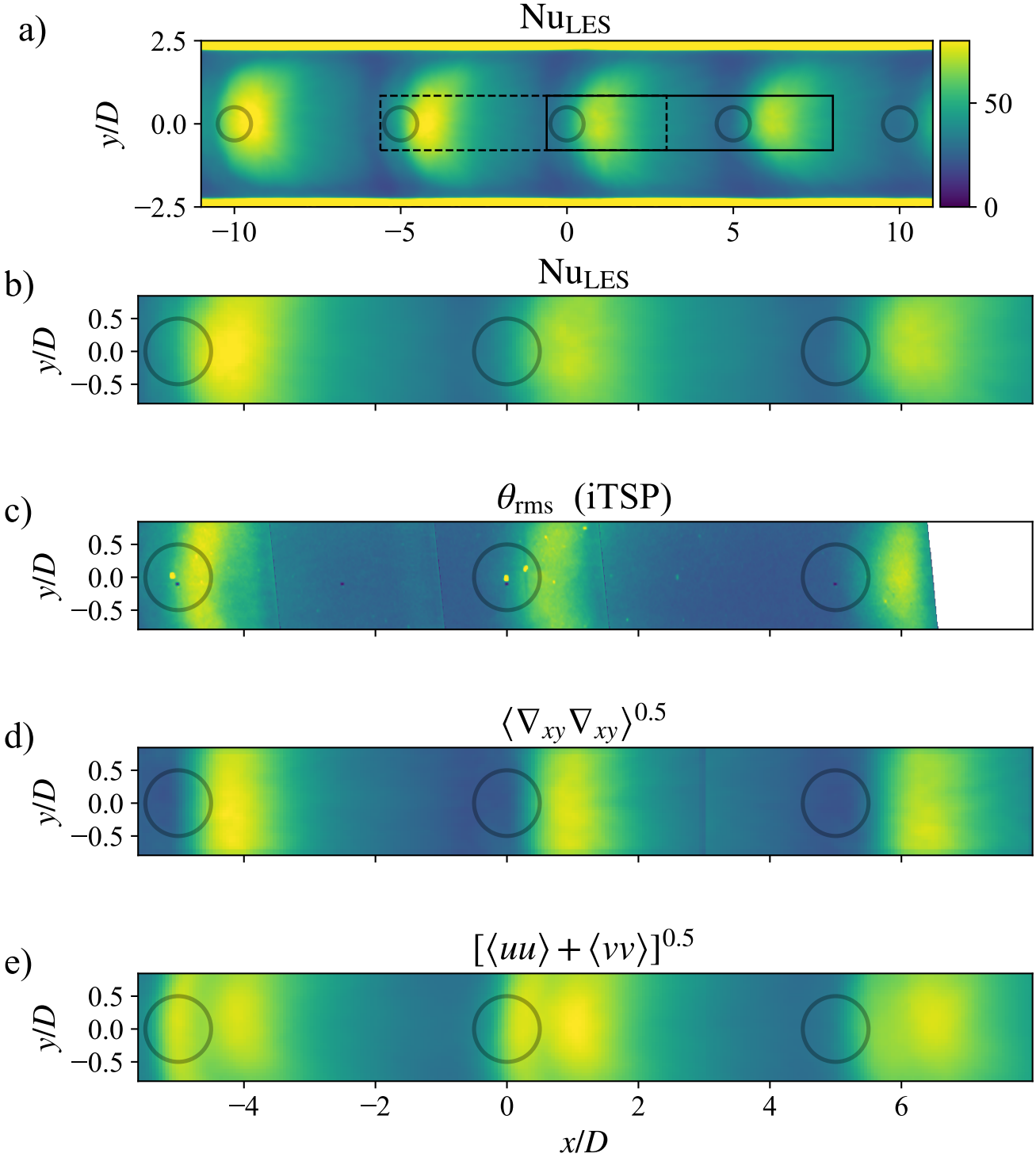

Figure 15. Nusselt number distribution below jet No. 5 to jet No. 9 obtained with LES (**a**); rectangles indicate TR-PIV sampling domains. Detail view of Nusselt distribution around jet No. 7 (**b**), standard deviation of temperature, θ_{rms} (**c**), standard deviation of ∇_{xy} (**d**), square root of sum of velocity variances obtained with TR-PIV (**e**).

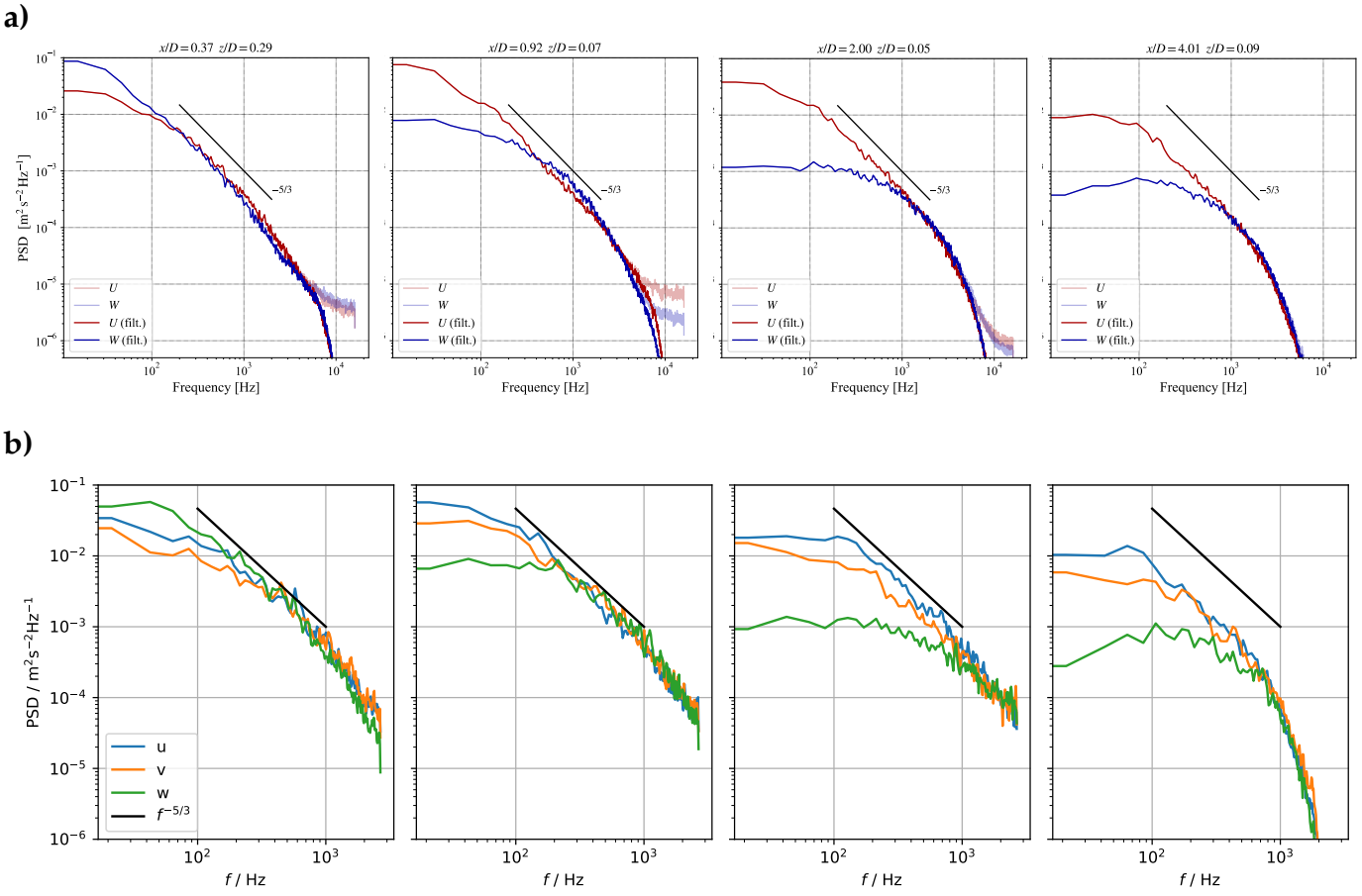

Figure 16. Power spectra of the near-wall velocity profiles at center-plane ($y = 0$) below jet No. 7 obtained with high-magnification TR-PIV (**a**) and LES (**b**) at the points indicated in Fig. 10.

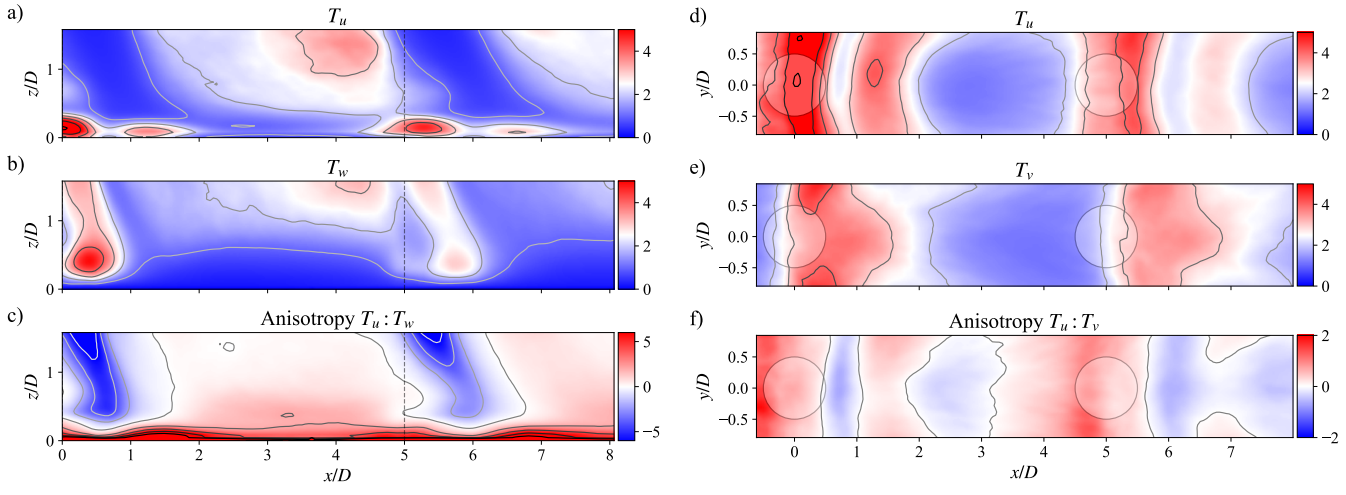

Figure 17. Normalized integral time scales near jet No. 7 and jet No. 8 in the xz-plane at $y = 0$ (left) and in the xy-plane at $z \approx 1$ mm for velocity components u (**a,d**), v (**e**), w (**b**) and measure of anisotropy (**c,f**), see text for definition). Contour levels are spaced by 1.0 for (**a,b,d,e**) and 2.0 for (**c,f**).

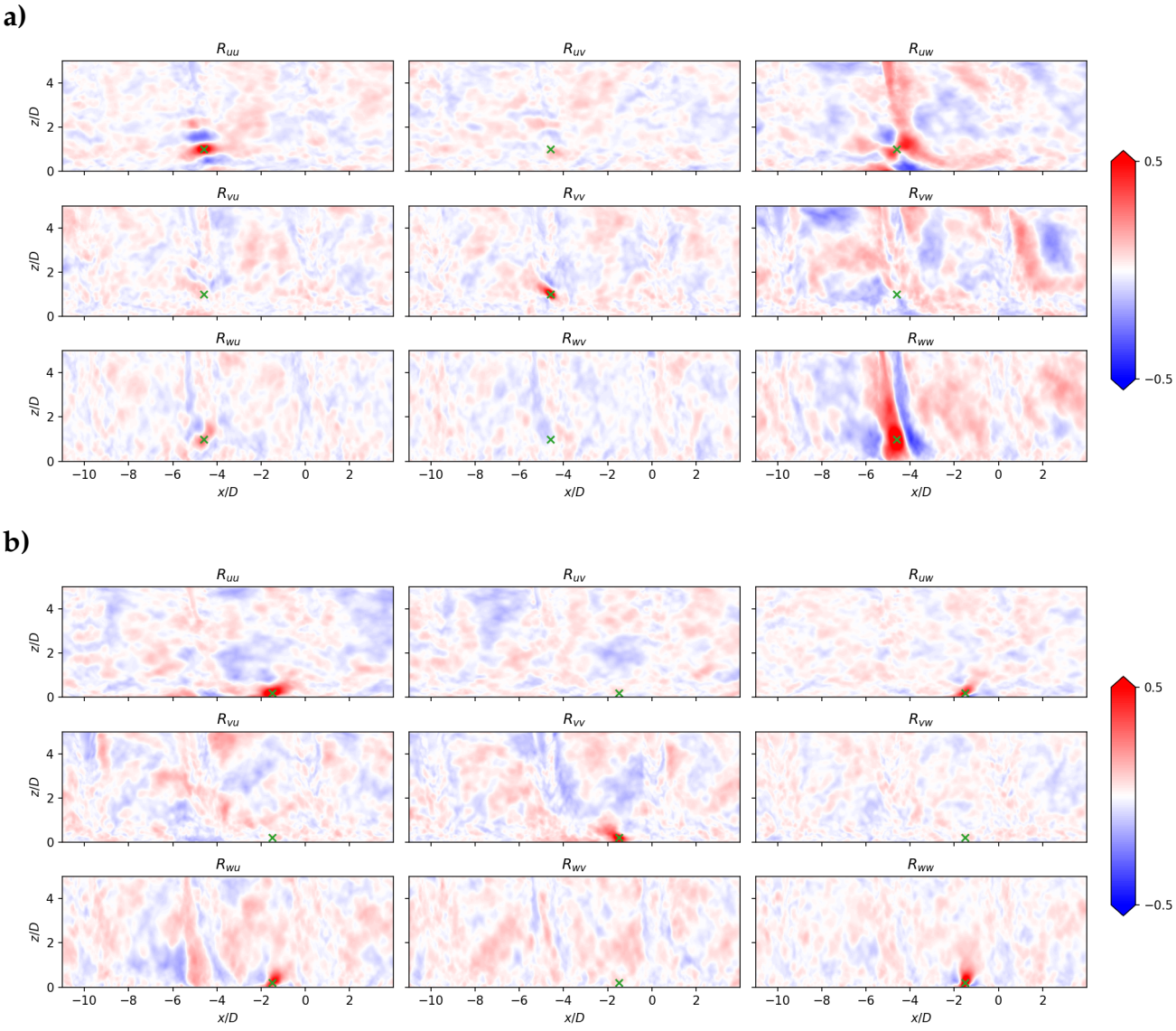

Figure 18. Two-point correlation maps from LES in the xz-plane averaged over the planes y/D = {-0.2, -0.1, 0.0, 0.1, 0.2} covering jet No. 5 to jet No. 7. Reference point chosen on streamline of jet No. 6 wall distance of $z/D = 1.0$ (a) and upstream of jet No. 7 at $z/D = 0.2$ (b).

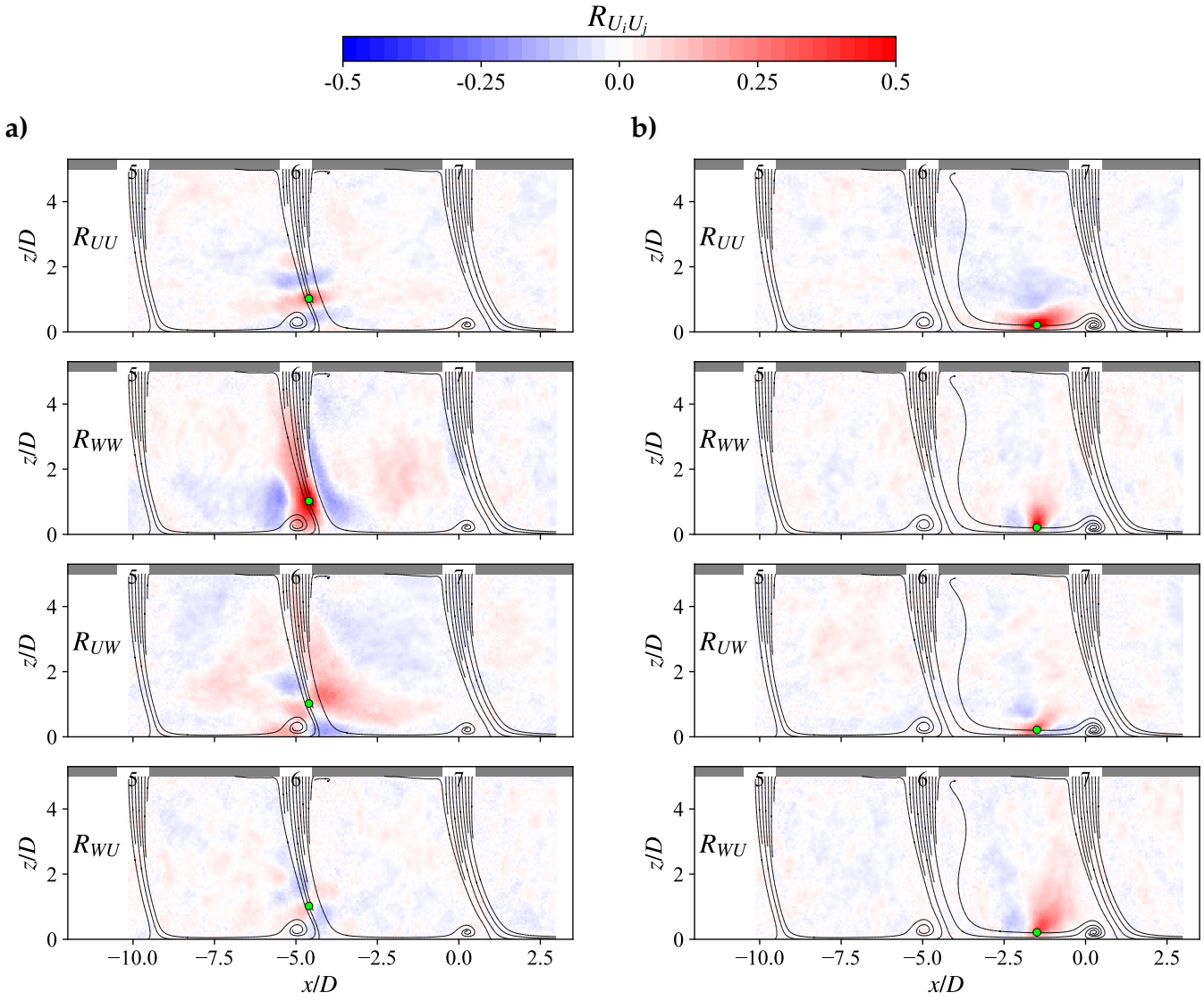

Figure 19. Two-point correlation maps in the xz-plane at $y = 0$ covering jet No. 5 to jet No. 7. Reference point chosen on streamline of jet No. 6 wall distance of $z/D = 1.0$ (a) and upstream of jet No. 7 at $z/D = 0.2$ (b).

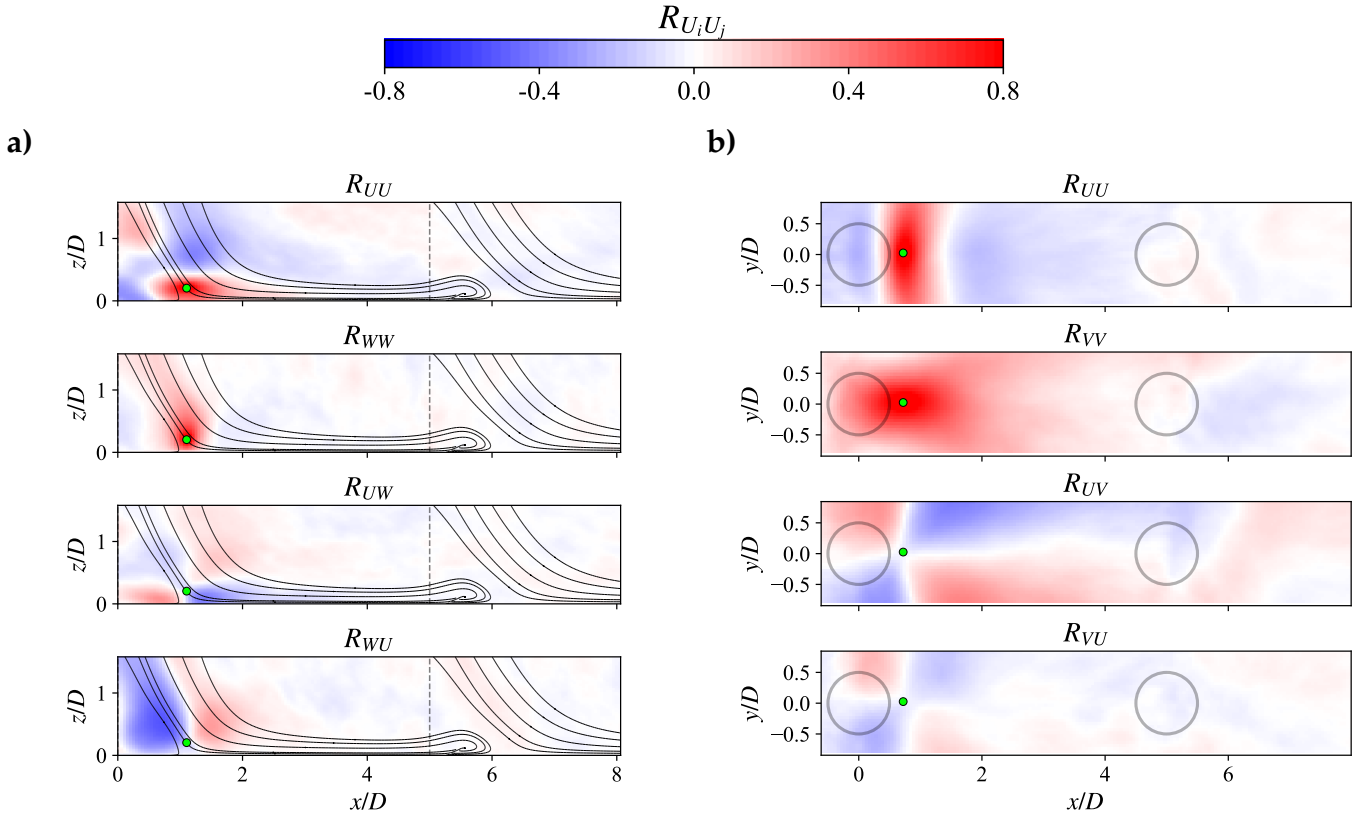

Figure 20. Two-point correlation maps in the xz-plane at $y = 0$ (**a**) and xy-plane (**b**).

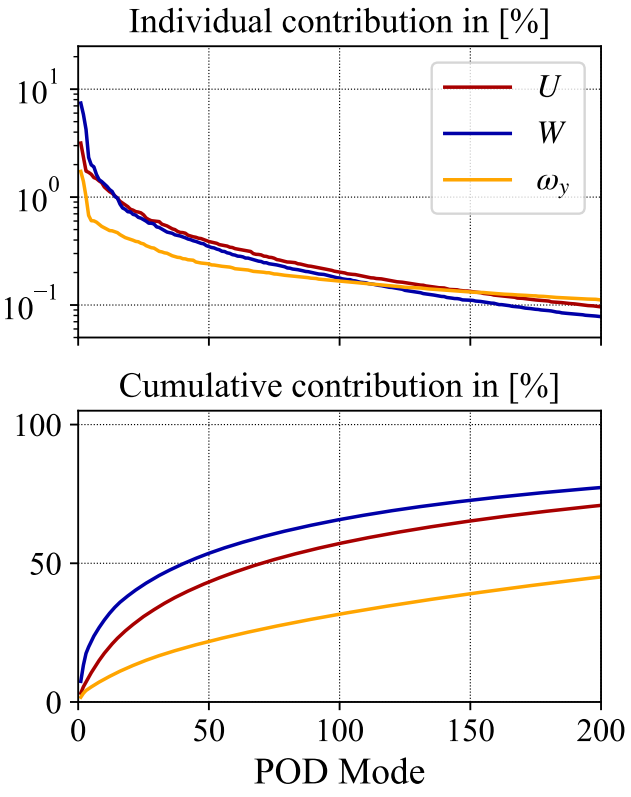

Figure 21. Relative and cumulative energy distribution of the POD modes for velocity components u, w and vorticity component ω_y in the xz-plane at $y = 0$ covering jet No. 5 to jet No. 7.

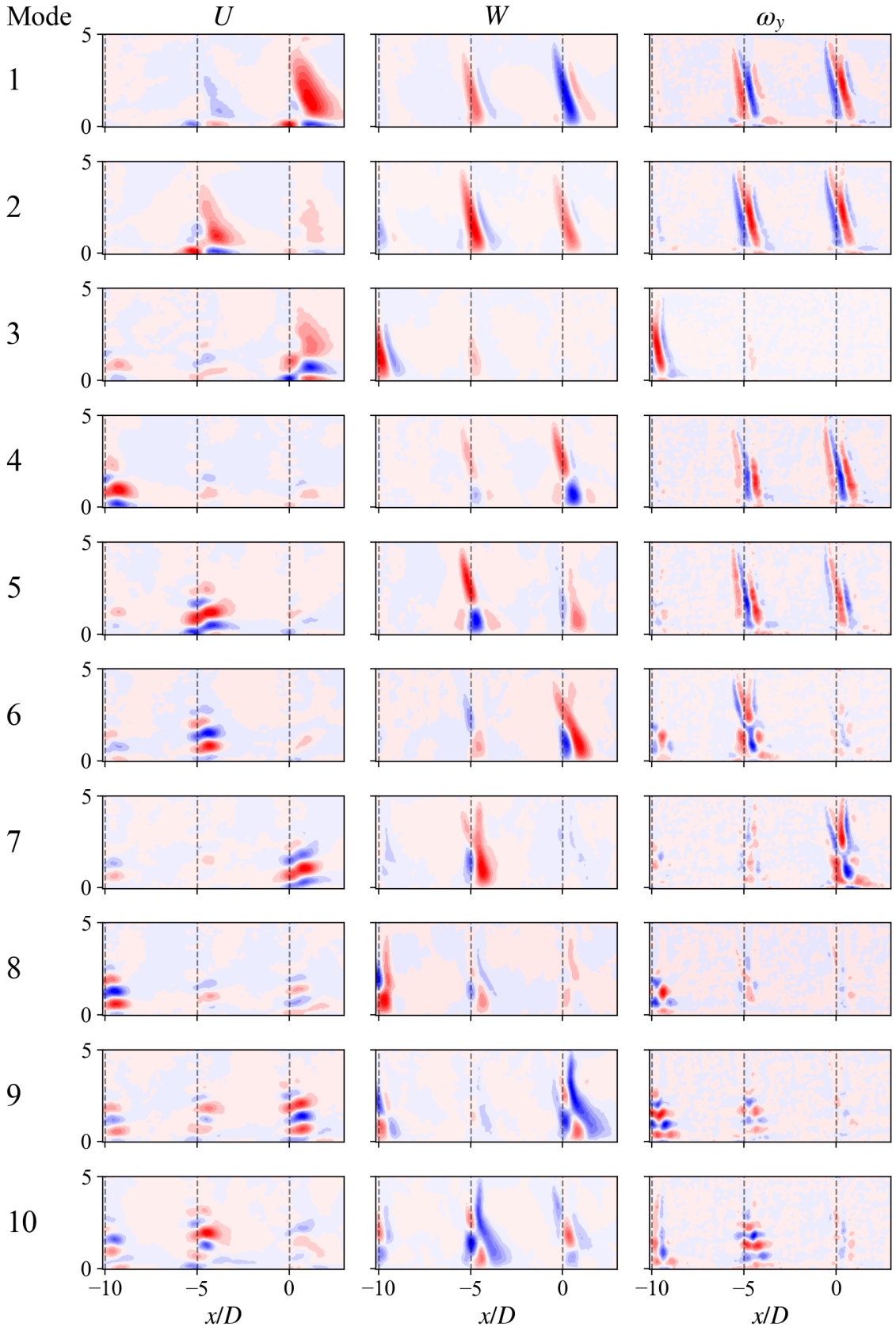

Figure 22. First 10 POD modes for velocity components u, w and vorticity component ω_y in the xz-plane at $y = 0$.

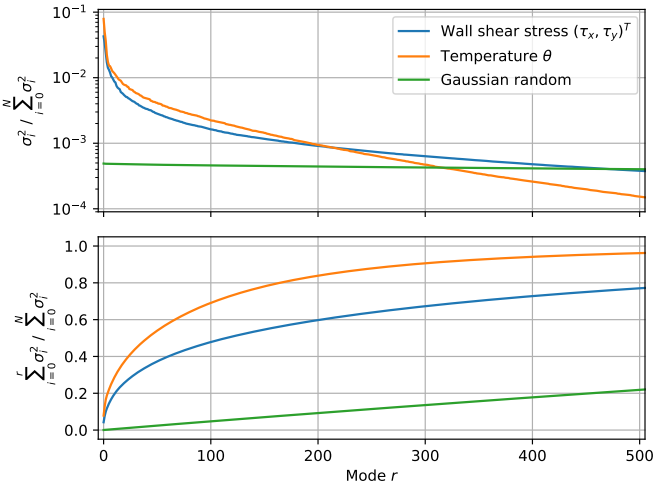

Figure 23. Relative and cumulative energy distribution of the POD modes for wall shear stress vector $(\tau_x, \tau_y)^T$ and temperature θ (independently) near jet No. 7 and jet No. 8 obtained with LES. Distribution of Gaussian random matrix serves to indicate noise threshold.

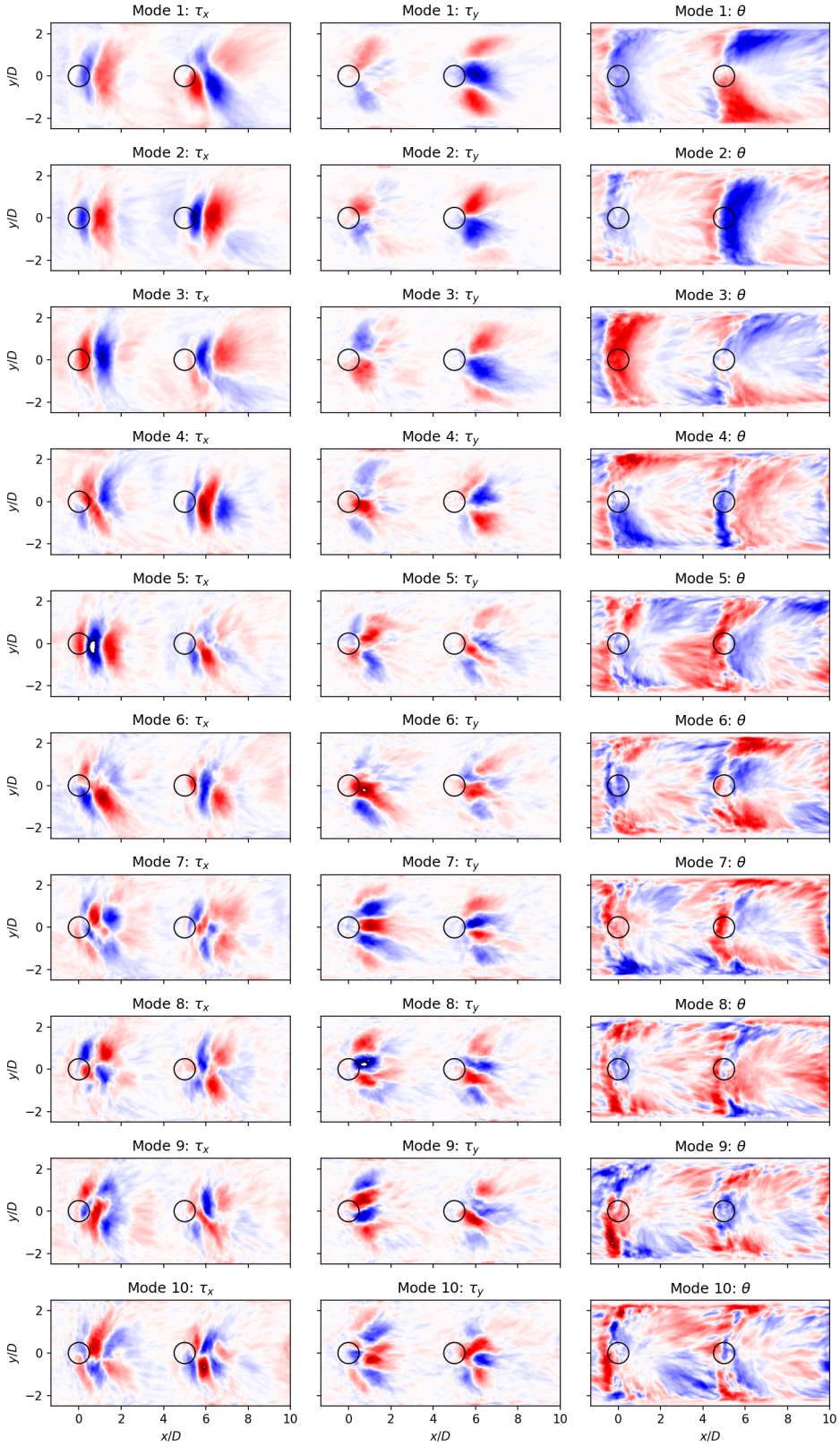

Figure 24. First 10 POD modes for wall shear stress components $\tau_{xy} = (\tau_x, \tau_y)^T$ and temperature θ (independently) near jet No. 7 and jet No. 8 obtained with LES.

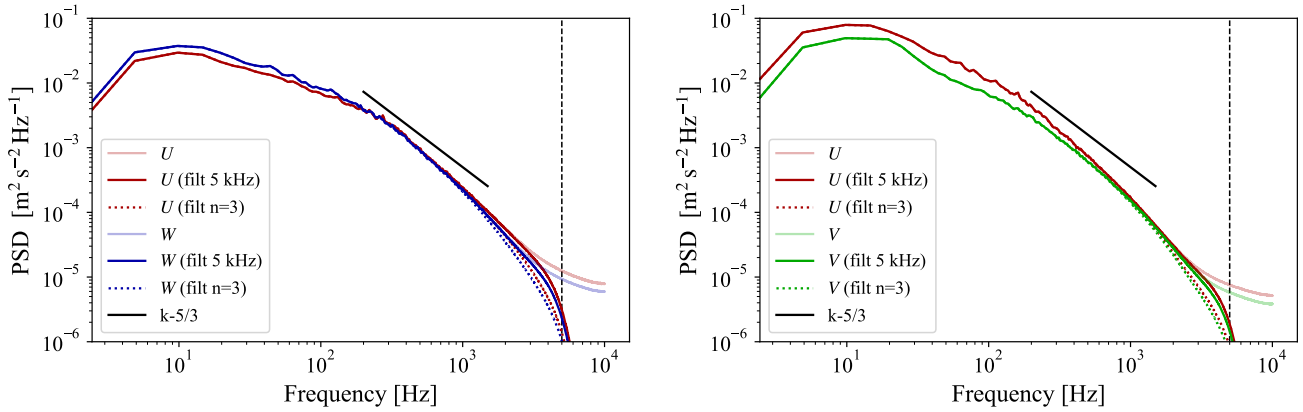

Figure 25. Mean power spectral density for the TR-PIV data obtained near jet No. 7 and jet No. 8 in the xz-plane at $y = 0$ (left) and xy-plane about 1 mm from the impingement wall. Spectra are shown for raw and temporally filtered velocity components with a cutoff frequency of $f_c = 5$ kHz.

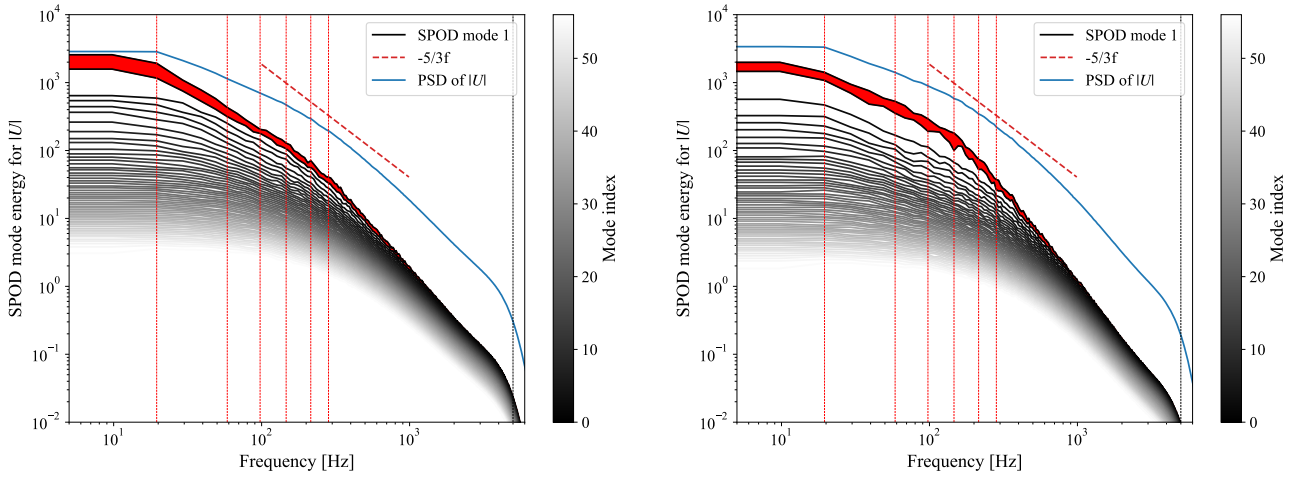

Figure 26. SPOD spectral density for velocity magnitude of the TR-PIV data obtained in the xz-plane at $y = 0$ (left) and xy-plane near jet No. 7 and jet No. 8.

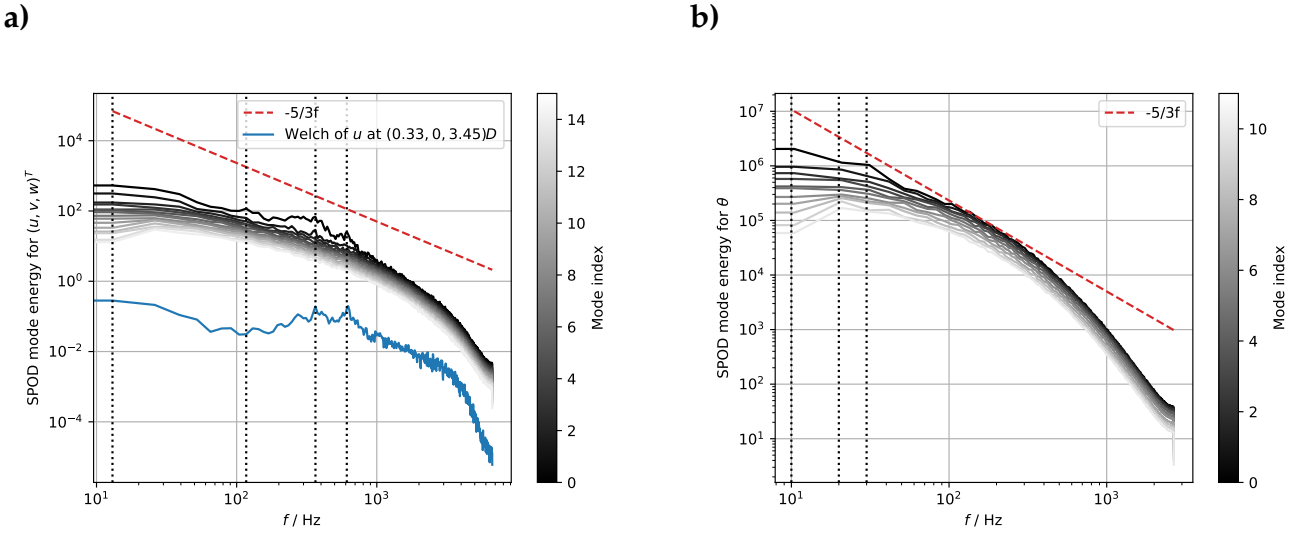

Figure 27. SPOD spectral density obtained with LES for velocity $(u, v, w)^T$ near jet No. 7 on the center-plane ($y = 0$, **a**) and for the temperature θ at the wall near jet No. 7 and jet No. 8 (**b**).

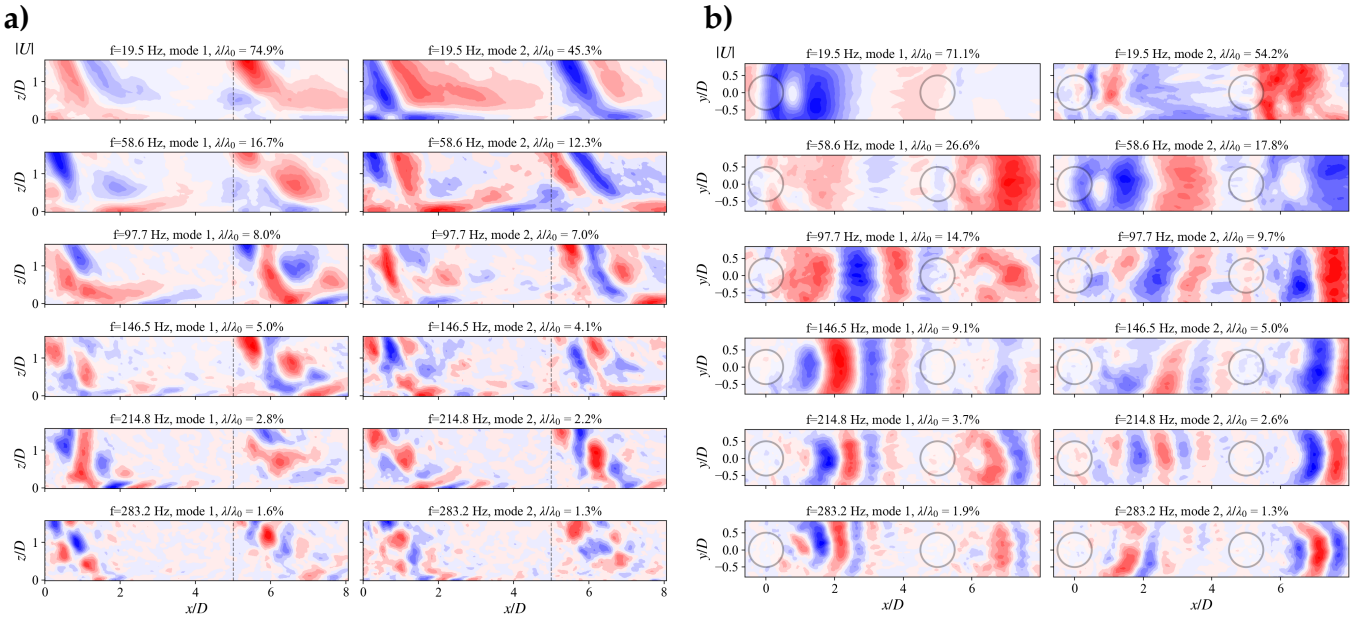

Figure 28. Selected SPOD modes for velocity magnitude of the TR-PIV data obtained near jet No. 7 and jet No. 8 in the xz-plane at $y = 0$ (**a**) and xy-plane (**b**).

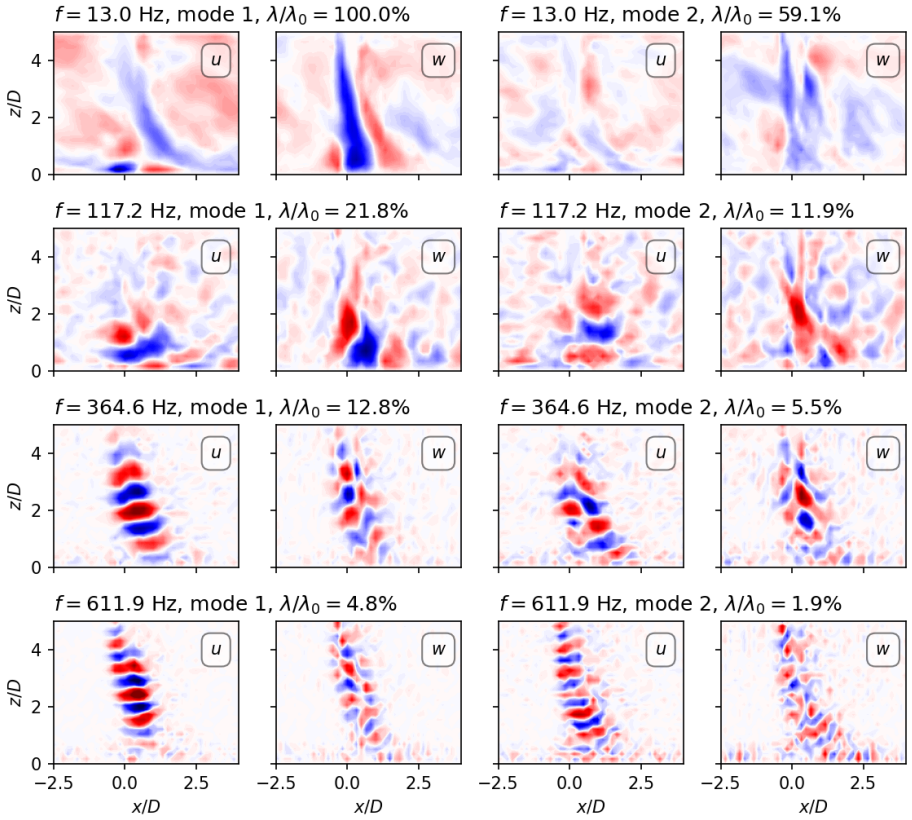

Figure 29. SPOD modes for velocity components u, w on the $y = 0$ plane obtained with LES near jet No. 7.

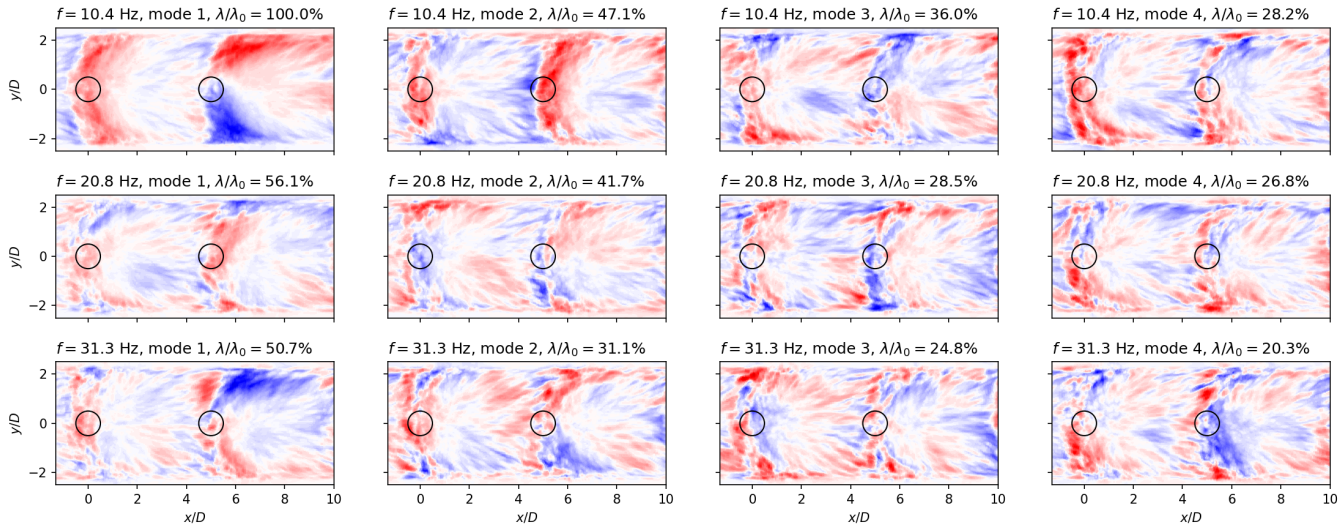

Figure 30. SPOD modes for temperature θ at the wall obtained with LES near jet No. 7 and jet No. 8.